


Theoretical study of extrinsic spin current generation in ferromagnets induced by anisotropic spin-flip scattering

Yuta Yahagi,^{*} Daisuke Miura, and Akimasa Sakuma

Department of Applied Physics, Tohoku University, Sendai, Miyagi, Japan

Jakub Železný

Institute of Physics, Academy of Sciences of Czech Republic, Prague, Czech Republic

 (Received 14 April 2021; revised 27 July 2021; accepted 31 August 2021; published 14 September 2021)

The spin Hall effect (SHE) is responsible for electrical spin current generation, which is a key concept of modern spintronics. We present a theoretical study of an extrinsic mechanism of SHE arising from a spin-dependent s - d scattering in ferromagnets. In order to investigate the spin conductivity in a ferromagnetic $3d$ alloy model, we employ a microscopic transport theory based on the Kubo formula and the averaged T -matrix approximation. From the model, we derived an extrinsic mechanism that contributes to both the SHE and the time-reversal odd SHE known as the magnetic SHE. This mechanism can be understood as the contribution from anisotropic (spatial-dependent) spin-flip scattering due to the combination of the orbital-dependent anisotropic shape of s - d hybridization and spin flipping, with the orbital shift caused by spin-orbit interaction with the d orbitals. We also show that this mechanism is valid under crystal-field splitting among the d orbitals in either the cubic or tetragonal symmetry.

DOI: [10.1103/PhysRevB.104.094417](https://doi.org/10.1103/PhysRevB.104.094417)

I. INTRODUCTION

The spin current is a central concept in recent spintronics, and many novel devices driven by the spin current have been proposed, including spin torque magnetic random access memory [1]. Importantly, the use of the spin current in practical applications requires the spin current to be generated efficiently. One of the most practical methods is the spin-transfer effect in ferromagnetic metal bilayers. However, because the spin transfer effect entails not only spin conduction but also charge conduction in principle, it damages the barrier layer, which is a bottleneck in the development of high-density memory [2,3].

The spin Hall effect (SHE) and inverse SHE are among the most promising methods for controlling spin currents in next-generation spintronics devices [4]. SHE is a phenomenon in which a spin current is generated perpendicular to the applied electric field in a material. Because the SHE can inject the spin current without a large current flowing through the barrier layer, it is expected to overcome the weakness of the spin transfer effect. SHE has been studied mainly in nonmagnetic heavy metals with a large spin-orbit interaction (SOI), such as Pt. Recently, however, the SHE in ferromagnetic metals (FMs) has attracted considerable attention [5–10]. Some measurements show that the SHE in FMs can generate sufficient spin current to induce magnetization switching with a spin conversion ratio comparable to that in Pt [11–16]. The spin swapping effect, a type of SHE that has a perpendicularly polarized spin current, is also enhanced in FMs [17,18].

Furthermore, spin-current generation owing to the planar Hall effect (PHE) [a transverse anisotropic magnetoresistance (AMR) effect], rather than the SHE, has also been shown to occur in ferromagnetic metals [11,19,20]. This PHE-driven spin current (PHE-SC) can also generate a large spin-orbit torque, as demonstrated in recent measurements [19,20]. The magnetic spin Hall effect (MSHE) and inverse MSHE, which are new types of charge-spin conversion phenomena, have been reported for a wide range of magnetic materials and have attracted much attention [21–25]. The MSHE is defined as the time-reversal odd (T-odd) spin-current generation effect; that is, its sign is inverted under a time-reversal operation, unlike the conventional SHE. According to this definition, the PHE-SC can be considered as a variant of the MSHE because the PHE-SC has T-odd symmetry as well. It should be emphasized that the MSHE differs from the spin-polarized current driven by the anomalous Hall effect (AHE), which must be a T-even spin current because of the restriction of the reciprocity theorem among the anomalous Hall conductivities. Although the AHE and the associated spin-current generation are driven by Lorentz forces owing to effective magnetic fields, such as Berry curvature, the MSHE is not. As discussed later, the redistribution of electrons by an applied electric field is essential for the MSHE, rather the effective magnetic fields.

From the perspective of device applications, these magnetization-induced SHE-like effects can have some advantages compared to SHE in nonmagnetic materials. For example, magnetic materials could reduce the use of precious metals. Moreover, the spin current in magnetic materials can be easily controlled by modifying the magnetic structure, whereas the spin current in nonmagnetic materials is restricted by either the symmetry of the material or the geometry of

^{*}yahagi@solid.apph.tohoku.ac.jp

the device. An additional advantage is that the spin current in magnetic materials is less constrained than that in non-magnetic materials because of the symmetry breaking arising from the magnetic structure. Magnetic materials can provide polarized spin current parallel to the flow direction, which is preferable for the spin-orbit torque switching of perpendicular magnetization.

When an electric field E_j is applied to a material, the response spin current J_i^μ is described as

$$J_i^\mu = \sigma_{ij}^\mu E_j, \quad (1)$$

where μ and i denote the spin polarization direction and flow direction of the spin current, respectively. The linear response tensor σ_{ij}^μ is referred to as a spin-conductivity tensor. We decompose σ_{ij}^μ by the time-reversal symmetry, and define the T-even term as the SHE with $\mathcal{T}\sigma^{\text{SHE}} = +\sigma^{\text{SHE}}$ and the T-odd term as the MSHE with $\mathcal{T}\sigma^{\text{MSHE}} = -\sigma^{\text{MSHE}}$ where \mathcal{T} denotes the time-reversal operation. For systems invariant under time-reversal symmetry, such as nonmagnetic materials, the relationship of $\mathcal{T}\sigma_{ij}^\mu = +\sigma_{ij}^\mu$ holds and the MSHE is forbidden. Therefore, MSHE can only appear in magnetic materials. The shape of the spin-conductivity tensor has already been determined by symmetry analysis with a general formalism of linear response theory [26,27]. While the symmetry analyses include all linear response contributions, we shall discuss individual mechanisms to gain more insight into the origin of the spin conduction.

The microscopic mechanisms of SHE in nonmagnetic materials have been understood with reference to the theory of the anomalous Hall effect (AHE) in ferromagnetic materials. The major contributions to the SHE are widely believed to be the intrinsic mechanism owing to the Berry curvature of the band structure [28] and the extrinsic mechanism due to impurity scattering under the influence of the SOI, as well as skew scattering [29] and the side jump [30]. Hereinafter, we refer to the SHE arising from the intrinsic, skew-scattering, and side-jump mechanisms as the conventional SHE.

In magnetic materials, σ_{ij}^μ cannot be fully explained by extending the AHE theory because of the existence of additional contributions. Recently, several measurements have shown a qualitative disagreement between the anomalous Hall resistivity and the spin Hall resistivity [31–33]. These results illustrate that the SHE is not always proportional to the AHE, as is sometimes believed, and suggest the breakdown of the two-current model or the existence of unidentified mechanisms.

The mechanism of the MSHE is not analogous to that of the AHE. From the viewpoint of Boltzmann transport theory, the MSHE can be expressed by an asymmetric nonequilibrium distribution of the electron spins at the spin-momentum locked Fermi surface, shifted by an external electric field [21]. Although previous studies on the MSHE have mainly focused on noncollinear antiferromagnets because this effect was initially predicted [21] and observed [22] in Mn_3Sn , the symmetry analysis shows that the MSHE can appear in a wide range of magnetic materials, including typical ferromagnetic metals [24,25]. The MSHE was also first predicted for bcc- Fe , assuming a simple estimation under the assumption of spin-independent scattering [21]. In actual ferromagnetic

metal systems, however, spin-dependent scattering can play a dominant role. The AMR effect is a typical phenomenon in which the contribution from spin-dependent scattering is more dominant than that from spin-independent scattering. As mentioned above, it has already been partially discussed in the study of the PHE-SC, a subset of the MSHE, under the assumption of the two-current model. However, spin currents driven by spin-polarized currents are only the secondary effects of a charge current response; thus, it is necessary to proceed beyond the two-current model to completely understand the spin-current response.

The purpose of this work is to investigate the spin-current response in ferromagnetic metals with special focus on the spin-dependent scattering effects. We consider a ferromagnetic 3d transition metal dilute alloy model by assuming that the atoms of the minority species are randomly distributed impurities and investigate the impurity s - d scattering in this model. The electronic structure is described within the framework of the impurity Anderson model [34], which contains the host-lattice Hamiltonian, impurity Hamiltonian, and their hybridization term. We identified all the components of the spin current by directly formulating the spin conductivity based on microscopic linear response theory. Consequently, we found a new extrinsic mechanism of electrical spin-current generation arising from anisotropic (spatial-dependent) spin-flip (ASF) scatterings, a type of spin-flip scattering that depends on the direction of the momentum of the electron. This ASF scattering mechanism can contribute both to the SHE and to the MSHE with spin polarization not only parallel but also perpendicular to the magnetization direction, which is a feature that distinguishes it from the spin currents due to spin-polarized AHE or PHE currents. Intuitively, the spin current from the ASF scattering can be expressed as spins with different spin angular momenta depending on their direction of motion during the impurity scattering processes, as shown in Fig. 1. This scattering process does not occur in an s - s scattering but can occur in the s - d scattering involving an SOI in the d -orbital states and the orbital-selective s - d transition. The SOI in d orbitals has two roles: spin-orbit mixing, which causes spin flipping and orbital splitting as an effective magnetic field. The orbital selectivity of the s - d transition reorients the spins in a different direction, of which the sign corresponds to the phase of the target d orbital. Consequently, the electrons moving in different directions receive different spin angular momenta. Thus, the ASF scattering induces a momentum imbalance of the nonequilibrium spin distribution, which can drive spin currents polarized both parallel and perpendicular to the magnetization direction. This mechanism is new in the sense of microscopic origin, but not necessarily in the sense of symmetry. Hereafter, we refer to the T-even contribution from the ASF as the ASF-SHE and to the T-odd contribution from the ASF as the ASF-MSHE.

The remainder of this paper is structured as follows. In Sec. II, we introduce a one-electron Hamiltonian to describe ferromagnetic dilute alloys in the impurity Anderson model and express the spin conductivity by using the Kubo-Streda formula [35]. In Sec. III, we present the results of perturbation analyses and numerical calculations. In addition, we provide a kinetic picture of ASF-SHE and MSHE. Finally, we summarize our findings in Sec. IV.

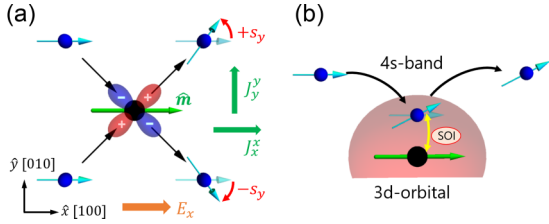


FIG. 1. (a) Real-space view of a spin-current induced by anisotropic spin-flip (ASF) scattering, s - d scattering involving an orbital-selective momentum-dependent spin-flip process. The blue spheres with arrows represent s electrons with their spins moving in the direction of the black arrows under the applied electric field E_x and the magnetization $\hat{m} \parallel \hat{x}$. The black spheres with red and blue ellipses represent an impurity with a d orbital. The colors correspond to the sign of the phase. For example, an electron moving in the $[1, 1, 0]$ direction is more likely to receive a net spin angular momentum $+s_y$ from a momentum-dependent spin flip, and vice versa for the electrons moving in the $[1, -1, 0]$ direction. Accordingly, not only is the longitudinal spin current J_x^x associated with the spin-polarized current, but also the transverse spin current J_y^y polarized perpendicular to the magnetization direction. (b) Schematic representation of a representative ASF scattering event. From a microscopic point of view, a momentum-dependent spin flip can be realized by a combination of the spin-orbit interaction (SOI) in the d orbitals and the selection rule for the s - d transition that connects the momentum and d orbital of the s electron. This means that the momentum and spin of an electron are coupled via intermediate d orbitals.

II. MODEL AND METHOD

In this study, we used two different coordinate systems, as shown in Fig. 2. The first is a stationary coordinate system with basis $\{\hat{x}, \hat{y}, \hat{z}\}$ and the other is a rotational coordinate system with respect to the magnetization vector with basis $\{\hat{\theta}, \hat{\phi}, \hat{m}\}$. These coordinate systems are connected by the following transformation:

$$\begin{aligned} & (\hat{\theta}, \hat{\phi}, \hat{m}) \\ &= (\hat{x}, \hat{y}, \hat{z}) \begin{pmatrix} \cos \theta_m \cos \phi_m & -\sin \phi_m & \sin \theta_m \cos \phi_m \\ \cos \theta_m \sin \phi_m & \cos \phi_m & \sin \theta_m \sin \phi_m \\ -\sin \theta_m & 0 & \cos \theta_m \end{pmatrix} \\ &\equiv (\hat{x}, \hat{y}, \hat{z})R \end{aligned} \quad (2)$$

with a three-dimensional rotation matrix R with respect to θ_m and ϕ_m , a polar angle and an azimuthal angle of a magnetization vector determined in the stationary coordinate system. For the sake of readability, we use Greek indices, such as μ, ν , and λ , for the rotational coordinate system and Roman indices, such as i, j , and n , for the stationary coordinate system. The

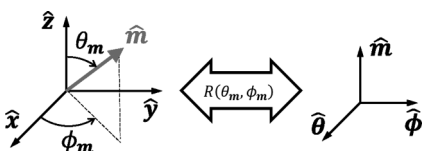


FIG. 2. Schematics of the coordination system of the stationary coordinate with the basis $\{\hat{x}, \hat{y}, \hat{z}\}$ and the rotational coordinate with respect to the magnetization direction \hat{m} with the basis $\{\hat{\theta}, \hat{\phi}, \hat{m}\}$.

Pauli matrices are defined as

$$\tilde{\sigma}_\theta = \begin{pmatrix} 0 & 1 \\ 1 & 0 \end{pmatrix}, \quad \tilde{\sigma}_\phi = \begin{pmatrix} 0 & -i \\ i & 0 \end{pmatrix}, \quad \tilde{\sigma}_m = \begin{pmatrix} 1 & 0 \\ 0 & -1 \end{pmatrix}, \quad (3)$$

and the spin basis $\{|\uparrow\rangle, |\downarrow\rangle\}$ is chosen from the eigenfunctions of $\tilde{\sigma}_m$. Hereinafter, all the operators represented by the 2×2 matrix in spin space, such as \tilde{A} , are distinguished by a tilde and the 2×2 identity matrix is denoted as $\tilde{\sigma}_0$.

Focusing on a ferromagnetic $3d$ transition metal dilute alloy, for simplicity, we consider a downfolded electron band containing $4s$ and $3d$ bands of the host lattice and localized states of the minority species. For the host-lattice system, we assume that the $4s$ band plays the role of conduction and is described by the electron gas model, whereas the $3d$ band plays the role of magnetization and is described by an effective magnetic field under a mean-field approximation. On the other hand, the localized states of the minority species are regarded as randomly distributed magnetic impurities, and their electronic states are described by localized atomic $3d$ orbitals. In such a situation, the electron Hamiltonian can be described as a multiorbital impurity Anderson model:

$$\tilde{H} = \tilde{H}_s + \tilde{H}_{\text{imp}} + \tilde{H}_{\text{hyb}} + \tilde{U}_{ss}, \quad (4)$$

where \tilde{H}_s is the conduction band Hamiltonian of the host-lattice system, \tilde{H}_{imp} is the atomic $3d$ orbital Hamiltonian of the impurity system, and \tilde{H}_{hyb} is the hybridization term. \tilde{U}_{ss} on the right-hand side of Eq. (4) represents the s - s scattering through the impurity potential and assumes a spin-independent delta function potential for a sufficiently short distance compared to the mean-free path of the conduction electrons. The conduction band can be described by

$$\tilde{H}_s = \sum_{\mathbf{k}} \frac{\hbar^2 k^2}{2m} c_{\mathbf{k}}^\dagger c_{\mathbf{k}} - \Delta_s \sum_{\mathbf{k}} (c_{\mathbf{k}}^\dagger \tilde{\sigma} c_{\mathbf{k}}) \cdot \hat{m}, \quad (5)$$

where $c_{\mathbf{k}} = (c_{\mathbf{k},\uparrow}, c_{\mathbf{k},\downarrow})^T$ and $c_{\mathbf{k}}^\dagger = (c_{\mathbf{k},\uparrow}^\dagger, c_{\mathbf{k},\downarrow}^\dagger)$ denote the creation and annihilation operators of conduction electrons with momentum \mathbf{k} and spin σ . $\tilde{\sigma} = (\tilde{\sigma}_\theta, \tilde{\sigma}_\phi, \tilde{\sigma}_m)$ is a vector representation of the Pauli matrices in Eq. (3). $\frac{\hbar^2 k^2}{2m}$ represents the kinetic energy of the conduction electron, and Δ_s is the strength of the exchange splitting from the ferromagnetic background. The Hamiltonian of the localized states in a scheme of the Hartree-Fock approximation (HFA) can be described by considering an exchange splitting, a SOI, and a crystal field as follows:

$$\begin{aligned} \tilde{H}_{\text{imp}} &= \sum_i^{N_{\text{imp}}} \sum_{M, M'=-2}^2 d_{i, M'}^\dagger \{ (E_{\text{imp}} \tilde{\sigma}_0 - \Delta_d \tilde{\sigma} \cdot \hat{m}) \delta_{M', M} \\ &\quad + \lambda [I]_{M', M} \cdot \tilde{\sigma} + (\tilde{V}_{\text{cf}})_{M', M} \} d_{i, M}, \end{aligned} \quad (6)$$

$$\begin{aligned} [\tilde{V}_{\text{cf}}]_{M', M} &= \frac{\Delta_C}{2} (\delta_{M', \pm 2} \delta_{M, \pm 2} + \delta_{M', \pm 2} \delta_{M, \mp 2} + \delta_{M', \pm 0} \delta_{M, \pm 0}) \\ &\quad + \Delta_T (\delta_{M', \pm 1} \delta_{M, \pm 1} + \delta_{M', \pm 0} \delta_{M, \pm 0}), \end{aligned} \quad (7)$$

where $d_{i, M} = (d_{i, M, \uparrow}, d_{i, M, \downarrow})^T$ and $d_{i, M}^\dagger = (d_{i, M, \uparrow}^\dagger, d_{i, M, \downarrow}^\dagger)$ denote the creation and annihilation operators of electrons on the $3d$ -orbital state on the impurity site i with the orbital magnetic quantum number M and spin σ . E_{imp} is the energy level

center of the impurity state measured from the bottom of the conduction band. We treat E_{imp} as an individual parameter that includes the uniform energy shift due to electron-electron correlation, instead of giving a specific electron configuration. Δ_d is the strength of the exchange splitting in the impurity state in the HFA, representing not only the intra-atomic electron correlation but also the contribution from the ferromagnetic molecular field created by the $3d$ bands of the surrounding host lattice. $\mathbf{l} = (l_x, l_y, l_z)$ denotes each component of the angular momentum operator belonging to azimuthal quantum number $L = 2$, and λ represents the coupling constant of the SOI. For the crystal field, we consider the case of cubic or tetragonal crystals and take the crystal axis as $(\hat{\mathbf{a}}, \hat{\mathbf{b}}, \hat{\mathbf{c}}) = (\hat{\mathbf{x}}, \hat{\mathbf{y}}, \hat{\mathbf{z}})$. Δ_C denotes the strength of the cubic field splitting. Although the strength of the tetragonal-field splitting is not exactly the same for each state, it is represented by a single parameter Δ_T for simplicity. Δ_T denotes the energy difference resulting from tetragonal distortion, that is, the deviation from cubic symmetry. Because each localized state is independent of the impurity position, \tilde{H}_{imp} can be divided into the on-site part \tilde{H}_d and a part representing the impurity configuration, written as

$$\tilde{H}_d \otimes \left(\sum_i^{N_{\text{imp}}} |i\rangle \langle i| \right). \quad (8)$$

The hybridization term between the conduction band and the localized state is expressed as

$$\tilde{H}_{\text{hyb}} = \frac{1}{\sqrt{\Omega}} \sum_i^{N_{\text{imp}}} \sum_{\mathbf{k}, M} (c_{\mathbf{k}}^\dagger e^{-i\mathbf{k}\cdot\mathbf{r}_i} \tilde{V}_{\mathbf{k}, M}^{\text{sd}} d_{i, M} + \text{H.c.}), \quad (9)$$

$$\tilde{V}_{\mathbf{k}, M}^{\text{sd}} = (\tilde{V}_{M, \mathbf{k}}^{\text{ds}})^\dagger = -\tilde{V}(k) Y_{2, M}(\hat{\mathbf{k}}), \quad (10)$$

$$\tilde{V}(k) = \begin{pmatrix} V_\uparrow(k) & 0 \\ 0 & V_\downarrow(k) \end{pmatrix}, \quad (11)$$

where \mathbf{r}_i is the position vector pointing to the impurity center, Ω is the volume of the system, $V_\sigma(k)$ is a radial function with spin σ , and $Y_{L, M}(\hat{\mathbf{k}})$ is a spherical harmonic in the k space. Here, we assume that spin mixing via an s - d transition event is negligibly small.

To treat the randomness of the impurities, we adopted a scattering T -matrix approach with a method based on the Green's function [36,37]. The s - s scattering is taken into account within the first Born approximation. For the s - d scattering, we treat this within the framework of the averaged T -matrix approximation in the dilute limit (DL-ATA), under the assumption that the interference between the impurities is negligible and the impurity concentration is sufficiently dilute. In addition, we exclude the scattering processes in which the s - s and s - d scattering interfere with each other. These approximations correspond to the disregard of, for example, the diagrams in Fig. 3. In such a case, the Green's function \tilde{G}_k of the conduction electron and its self-energy $\tilde{\Sigma}_k$ can be expressed as shown in Fig. 4,

$$\tilde{G}_k^\pm(E) = \{E\tilde{\sigma}_0 - \tilde{H}_s - \tilde{\Sigma}_k^\pm(E)\}^{-1}, \quad (12)$$

$$\tilde{\Sigma}_k^\pm(E) = \langle \tilde{T}_{k, k}^\pm \rangle_{\text{conf}} \pm i\eta_{ss}\tilde{\sigma}_0, \quad (13)$$

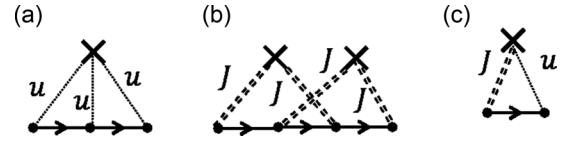


FIG. 3. Representative terms of the diagrams excluded from this work. (a) Higher-order Born terms of s - s scattering. (b) Crossing diagrams corresponding to quantum interference between multiple impurities. (c) On-site interference between s - s and s - d scattering terms.

where \tilde{G}_k or $\tilde{\Sigma}_k$ with $+$ ($-$) corresponds to the retarded (advanced) Green's function or self-energy and takes an appropriate sign depending on its own analyticity. η_{ss} is a positive real constant corresponding to the magnitude of s - s scattering and describes the constant spectral broadening of the conduction band. $\langle \tilde{A} \rangle_{\text{conf}}$ denotes the configurational average of \tilde{A} of the impurity; therefore, $\langle \tilde{T}_{k, k} \rangle_{\text{conf}}$ represents the configurational average T matrix of the s - d scattering. Using $N_{\text{imp}} \gg 1$, $\langle \tilde{T}_{k, k} \rangle_{\text{conf}}$ is approximately equal to the self-energy from the s - d scattering contribution.

Applying the DL-ATA, we obtain

$$\langle \tilde{T}_{k, k'} \rangle_{\text{conf}} \simeq n_{\text{imp}} \tilde{t}_{k, k'}(E), \quad (14)$$

where $\tilde{t}_{k, k'}(E)$ is a T matrix of single-site scattering, that is, the repeated scattering by the same impurity. For the impurity Anderson model, $\tilde{t}_{k, k'}(E)$ can be derived as

$$\begin{aligned} \tilde{t}_{k', k}^\pm(E) &= \sum_{M, M'} Y_{2, M'}^*(\hat{\mathbf{k}}') Y_{2, M}(\hat{\mathbf{k}}) \tilde{V}(k') \\ &\times [E\tilde{\sigma}_0 \delta_{M', M} - \tilde{H}_d - \tilde{\Sigma}_d^\pm(E)]_{M', M}^{-1} \tilde{V}(k), \end{aligned} \quad (15)$$

$$\cdot [\tilde{\Sigma}_d^\pm(E)]_{M', M} = \sum_k \tilde{V}_{M', k}^{\text{ds}} \tilde{G}_k^\pm(E) \tilde{V}_{k, M}^{\text{sd}}. \quad (16)$$

The diagrammatic expression of $\tilde{t}_{k, k'}(E)$ is shown in Fig. 5(a). It has almost the same form as the T matrix of the single impurity Anderson model except that in the case of multiple impurities, it includes a clothed Green's function \tilde{G}_k

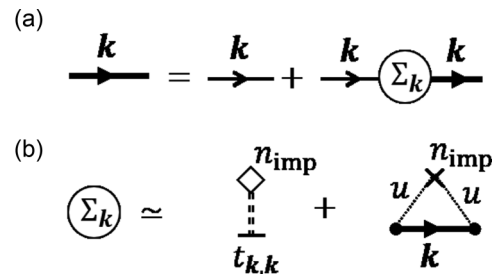


FIG. 4. Diagrammatic representations of (a) Dyson's equation for Green's function and (b) the self-energy of the conduction electron. (a) The bold lines represent the clothed Green's function, and the thin line represents the bare one. (b) Self-energy approximated by the configuration-averaged s - d and s - s scattering T matrix. The double-dashed line represents the s - d scattering, and the dotted line represents the s - s scattering. The point marked by a cross represents a coherent scattering event by a single impurity, whereas the point marked by a diamond represents the scattering by the renormalized effective potential, including all single-site scattering processes.

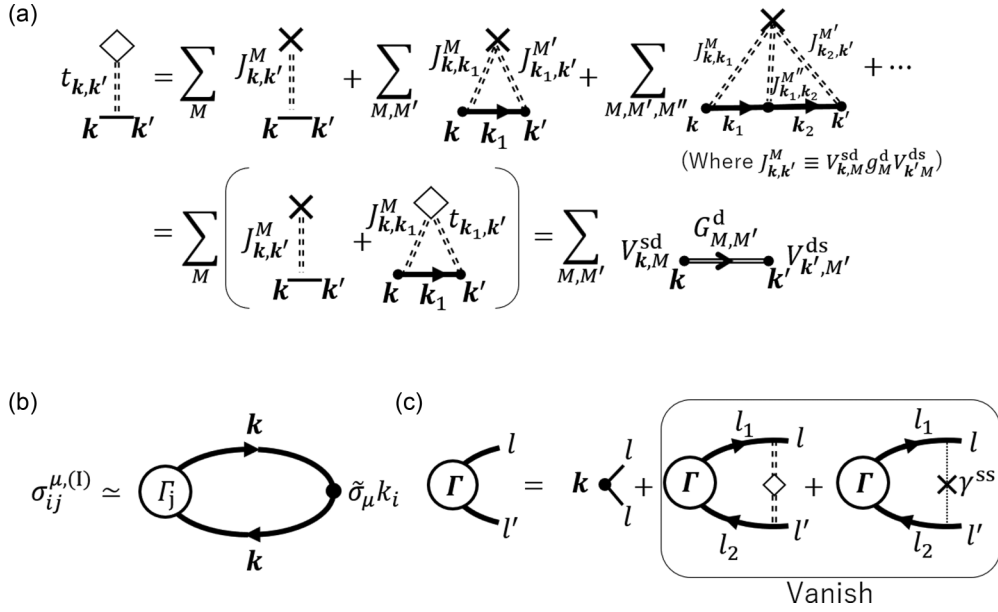


FIG. 5. Diagrammatic representation of (a) the single-site s - d scattering T matrix in the dilute limit averaged T -matrix approximation, (b) the current-spin-current correlation function for the Fermi-surface term in the Kubo-Streda formula, and (c) the Bethe-Salpeter equation (BSE) of the current vertex function. Here, $\tilde{g}^{\text{d}} \equiv (E\tilde{\sigma}_0 - \tilde{H}_{\text{d}})^{-1}$ represents the bare Green's function of the impurity system, and $\tilde{G}^{\text{d}} \equiv (E\tilde{\sigma}_0 - \tilde{H}_{\text{d}} - \tilde{\Sigma}_{\text{d}})$ represents the clothed function. The second and third terms on the right-hand side of (c) vanish owing to the symmetry consideration of the s - d and s - s scattering as $\Gamma_{l,l'}(-k) = -\Gamma_{l,l'}(k)$, which leads to $\sum_k \Gamma_{l,l'}(k)f(k) = 0$. Therefore, the current vertex function can be replaced by a bare current operator. For this reason, although the T matrix in (a) includes higher-order terms than Born approximation, the skew-scattering terms contribute neither charge- nor spin-conduction in this work.

instead of a bare one \tilde{g}_k . For simplicity, we approximate $[\tilde{\Sigma}_{\text{d}}^{\pm}(E)]_{M',M} \rightarrow \pm i\eta_{\text{d}}\tilde{\sigma}_0\delta_{M',M}$ by introducing a positive real constant, η_{d} . We do not expect this approximation to have a major influence on the results of this work.

Each component of the spin conductivity tensor σ_{ij}^{μ} is given by the so-called Kubo-Streda formula [35]

$$\sigma_{ij}^{\mu} = \sigma_{ij}^{\mu(1)} + \sigma_{ij}^{\mu(II)}, \quad (17a)$$

$$\begin{aligned} \sigma_{ij}^{\mu(1)} &= \frac{\hbar}{4\pi\Omega} \text{Tr} \left\{ J_i^{\mu} \{ \tilde{g}_k^{+}(E_{\text{F}}) - \tilde{g}_k^{-}(E_{\text{F}}) \} \tilde{J}_j^0 \tilde{g}_k^{-}(E_{\text{F}}) \right. \\ &\quad \left. - \tilde{J}_i^{\mu} \tilde{g}_k^{+}(E_{\text{F}}) \tilde{J}_j^0 \{ \tilde{g}_k^{+}(E_{\text{F}}) - \tilde{g}_k^{-}(E_{\text{F}}) \} \right\}_{\text{conf}}, \quad (17b) \end{aligned}$$

$$\begin{aligned} \sigma_{ij}^{\mu(II)} &= -\frac{\hbar}{4\pi\Omega} \int_{-\infty}^{E_{\text{F}}} dE \text{Tr} \left\{ \tilde{J}_i^{\mu} \{ \tilde{g}_k^{-}(E) \}^2 \tilde{J}_j^0 \tilde{g}_k^{-}(E) \right. \\ &\quad \left. - \tilde{J}_i^{\mu} \tilde{g}_k^{-}(E) \tilde{J}_j^0 \{ \tilde{g}_k^{-}(E) \}^2 + \tilde{J}_i^{\mu} \tilde{g}_k^{+}(E) \tilde{J}_j^0 \{ \tilde{g}_k^{+}(E) \}^2 \right. \\ &\quad \left. - \tilde{J}_i^{\mu} \{ \tilde{g}_k^{+}(E) \}^2 \tilde{J}_j^0 \tilde{g}_k^{+}(E) \right\}_{\text{conf}}. \quad (17c) \end{aligned}$$

Here, we assume that the Fermi distribution function of the electron is given by the unit step function, which corresponds to the zero-temperature limit. \tilde{J}_i^0 represents the charge current operator, and $\tilde{J}_i^{\mu \neq 0} \equiv -(\hbar/4e)\{\tilde{J}_i^0, \tilde{\sigma}_\mu\}$ represents an operator of the spin current polarized in the μ direction. Here $\{\tilde{A}, \tilde{B}\}$ denotes an anticommutator. The charge- and spin-current operators contain a velocity term derived from the hybridization Hamiltonian, that is, $\partial\tilde{H}_{\text{hyb}}/\partial p_i$, which is known to contribute to the side-jump mechanism [38–40]. However, because the side-jump mechanism is not the focus of our work, we exclude this term; thus, we set the charge- and spin-current operators

to

$$\tilde{J}_i^0 = -e\frac{\hbar k_i}{m}\tilde{\sigma}_0, \quad \tilde{J}_i^{\mu} = \frac{\hbar^2 k_i}{2m}\tilde{\sigma}_\mu. \quad (18)$$

The current vertex correction for the configuration average is considered only for the terms containing $\langle \tilde{G}^{\pm} \tilde{J}_i^0 \tilde{G}^{\mp} \rangle_{\text{conf}}$ because these terms are typically much more dominant in metals than in other terms such as $\langle \tilde{G}^{\pm} \tilde{J}_i^0 \tilde{G}^{\pm} \rangle_{\text{conf}}$. Therefore, in this work, the vertex correction appears for $\sigma_{ij}^{\mu(1)}$, and the Bethe-Salpeter equation (BSE) for the current vertex $-(e\hbar/m)\tilde{\Gamma}_{k,k'}$ is expressed as

$$\begin{aligned} [\tilde{\Gamma}_{k,k'}^{\pm}]_{\alpha,\beta} &= \delta_{k',k}\delta_{\beta,\alpha}\mathbf{k} + n_{\text{imp}}^2 \sum_{\{k_i\}, \{s_i\}} [\tilde{\Gamma}_{k_1,k_2}^{\pm}]_{s_1,s_2} \\ &\quad \times [\tilde{G}_{k_1}^{\pm}]_{s_1,s_3} [\tilde{G}_{k_2}^{\mp}]_{s_2,s_4} [\tilde{\Gamma}_{k_1,k}^{\pm}]_{s_3,\alpha} [\tilde{\Gamma}_{k_2,k'}^{\mp}]_{s_4,\beta} \\ &\quad + \gamma^{\text{ss}} \sum_{k,k',s,s'} [\tilde{\Gamma}_{k,k'}^{\pm}]_{s,s'} [\tilde{G}_{k'}^{\pm}]_{s,\alpha} [\tilde{G}_{k'}^{\mp}]_{s',\beta}, \quad (19) \end{aligned}$$

with the abbreviation for (E) in each term. The diagrammatic expressions of $\sigma_{ij}^{\mu(1)}$ and BSE are shown in Figs. 5(b) and 5(c). The second and third terms on the right-hand side of Eq. (19) correspond to the vertex corrections from s - d and s - s scattering, respectively. The s - s scattering vertex function γ^{ss} is a constant. The symmetry considerations show that these vertex corrections vanish after taking the momentum integration because both integrands from the s - d and s - s scattering are odd functions with respect to \mathbf{k} as $kY_{L,M}^*(\hat{\mathbf{k}}')Y_{L,M}(\hat{\mathbf{k}})$ for $(L = 0, 2)$ [41].

Eventually, the configurational averaged response function can be obtained by replacing $\tilde{g}_k \rightarrow \tilde{G}_k$ and is derived as

$$\sigma_{ij}^{\mu,(I)} = A_\mu \left(\frac{\hbar^2}{m} \right)^2 \frac{1}{(2\pi)^3} \int d^3k k_i k_j \text{ReTr}_\sigma \tilde{\sigma}_\mu \times \{ \tilde{G}_k^+(E_F) \tilde{G}_k^-(E_F) - \tilde{G}_k^+(E_F) \tilde{G}_k^+(E_F) \}, \quad (20a)$$

$$\sigma_{ij}^{\mu,(II)} = A_\mu \left(\frac{\hbar^2}{m} \right)^2 \frac{1}{(2\pi)^3} \int d^3k \int_{-\infty}^{E_F} dE k_i k_j \text{ReTr}_\sigma \tilde{\sigma}_\mu \times [\tilde{G}_k^+(E), -\tilde{G}_k^+(E) \tilde{G}_k^+(E)]. \quad (20b)$$

A_μ is the coefficient of charge conductivity $A_0 = e^2/h$ for $\mu = 0$, and the coefficient of spin conductivity $A_\mu = -e/4\pi$ otherwise. Both $\sigma_{ij}^{\mu,(I)}$ and $\sigma_{ij}^{\mu,(II)}$ do not change their sign under the permutation of the direction ($i \leftrightarrow j$); therefore, the resultant spin conductivity tensor is a symmetric tensor. Note that the skew-scattering contribution does not appear in this expression because Eq. (20) consists only of the coherent term owing to the absence of the vertex correction. Skew scattering as a result of vertex correction is known to appear when considering the scattering between states with different parity, such as d - p scattering [38,39,42–44]. The side-jump contribution does not appear because it re-

quires relativistic corrections in the current operators [45], which is not considered in Eq. (18). In addition, the intrinsic mechanism disappears in Eq. (20) because the conduction band is assumed to consist only of s electrons, where the SOI does not take any effect unless the d -orbital SOI of the impurity is induced extrinsically. Thus, we emphasize that all of the conventional mechanisms (intrinsic, skew scattering, and side jump) are excluded from Eq. (20). In addition, the spin swapping effects are also excluded because they have the same origins that are associated with the conventional mechanisms of the SHE [17,18,46]. Hence all the contributions that we study in this work arise from novel mechanisms.

III. CALCULATION RESULTS

A. Perturbative analysis

In this section, we derive an analytical expression for the spin conductivity tensor σ_{ij}^μ in this model and determine its microscopic mechanism by taking a perturbation expansion with respect to the SOI. For simplicity, the crystal fields are disregarded in this section; thus $\Delta_C = \Delta_T = 0$. The nonperturbative terms of the d -orbital Green's function are represented as

$$\tilde{\Upsilon}^\pm(E) = \begin{pmatrix} \Upsilon_\uparrow^\pm(E) & 0 \\ 0 & \Upsilon_\downarrow^\pm(E) \end{pmatrix} \equiv \begin{pmatrix} (E - E_{\text{imp}} + \Delta_d \mp i\eta_d)^{-1} & 0 \\ 0 & (E - E_{\text{imp}} - \Delta_d \mp i\eta_d)^{-1} \end{pmatrix}. \quad (21)$$

Hereinafter, their arguments are abbreviated.

After taking the perturbation up to the 2nd order with respect to the SOI coupling constant λ , the single-site T matrix $\tilde{t}_{k,k}$ in Eq. (14) can be expanded as

$$\tilde{t}_{k,k} \simeq \tilde{t}_0 + \tilde{t}'_0 + \tilde{t}'_\parallel + \tilde{t}'_\perp, \quad (22a)$$

$$\tilde{t}_0 = \frac{5}{4\pi} \begin{pmatrix} V_\uparrow^2 \Upsilon_\uparrow & 0 \\ 0 & V_\downarrow^2 \Upsilon_\downarrow \end{pmatrix}, \quad (22b)$$

$$\tilde{t}'_0 = \frac{15}{4\pi} \lambda^2 (\Upsilon_\uparrow + \Upsilon_\downarrow) \begin{pmatrix} V_\uparrow^2 \Upsilon_\uparrow^2 & 0 \\ 0 & V_\downarrow^2 \Upsilon_\downarrow^2 \end{pmatrix}, \quad (22c)$$

$$\tilde{t}'_\parallel = -\frac{15}{4\pi} \lambda^2 (\Upsilon_\uparrow - \Upsilon_\downarrow) \begin{pmatrix} V_\uparrow^2 \Upsilon_\uparrow^2 & 0 \\ 0 & -V_\downarrow^2 \Upsilon_\downarrow^2 \end{pmatrix} \hat{k}_m^2, \quad (22d)$$

$$\tilde{t}'_\perp = -\frac{15}{4\pi} \lambda^2 V_\uparrow V_\downarrow \Upsilon_\uparrow \Upsilon_\downarrow (\Upsilon_\uparrow - \Upsilon_\downarrow) (\tilde{\sigma}_\theta \hat{k}_\theta + \tilde{\sigma}_\phi \hat{k}_\phi) \hat{k}_m, \quad (22e)$$

where \tilde{t}_0 is the nonperturbative term, and the remainder are the perturbed terms. Among the perturbed terms, \tilde{t}'_0 represents the isotropic parts with respect to the momentum vector \mathbf{k} , whereas \tilde{t}'_\parallel and \tilde{t}'_\perp represent the spin-diagonal and off-diagonal parts of the anisotropic ($\hat{\mathbf{k}}$ -dependent) terms, respectively. By substituting these terms into Eq. (12), \tilde{G}_k are expanded as

$$\tilde{G} \simeq \tilde{G}_0 + n_{\text{imp}} \tilde{G}_0 (\tilde{t}'_0 + \tilde{t}'_\parallel + \tilde{t}'_\perp) \tilde{G}_0, \quad (23)$$

where $\tilde{G}_0 \equiv (E \tilde{\sigma}_0 - \tilde{H}^s - n_{\text{imp}} \tilde{t}_0 \mp i\eta_{\text{ss}})^{-1}$ is the nonperturbative term of the Green's function. We substitute this equation in Eq. (20). Using the isotropic shape of \tilde{G}_0 in the momentum space, we integrate Eq. (20) by part on the spherical surface and the radius as

$$\sigma_{\mu\nu}^\theta = \sigma_\perp^{(\text{odd})} \left(\frac{15}{4\pi} \right) I[\hat{k}_\theta \hat{k}_m \hat{k}_\mu \hat{k}_\nu] - \sigma_\perp^{(\text{even})} \left(\frac{15}{4\pi} \right) I[\hat{k}_\phi \hat{k}_m \hat{k}_\mu \hat{k}_\nu], \quad (24a)$$

$$\sigma_{\mu\nu}^\phi = \sigma_\perp^{(\text{odd})} \left(\frac{15}{4\pi} \right) I[\hat{k}_\phi \hat{k}_m \hat{k}_\mu \hat{k}_\nu] + \sigma_\perp^{(\text{even})} \left(\frac{15}{4\pi} \right) I[\hat{k}_\theta \hat{k}_m \hat{k}_\mu \hat{k}_\nu], \quad (24b)$$

$$\sigma_{\mu\nu}^m = \sigma_\parallel^{(\text{odd})} \left(\frac{15}{4\pi} \right) I[\hat{k}_\mu \hat{k}_\nu \hat{k}_m^2] + \delta_{\mu,\nu} \tilde{\sigma}, \quad (24c)$$

where $I[f(\hat{\mathbf{k}})] \equiv \int_{\text{u.s.}} d\hat{\mathbf{k}} f(\hat{\mathbf{k}})$ is a surface integral on the unit sphere with respect to the momentum direction, $\bar{\sigma}$ is the unperturbed term of spin conductivity, and $\sigma_{\perp}^{(\text{odd})}$, $\sigma_{\perp}^{(\text{even})}$, and $\sigma_{\parallel}^{(\text{odd})}$ are the remaining parts including a radial integral of a momentum vector, which will be discussed later. The subscripts \parallel and \perp denote the spin polarization direction of the spin current parallel or perpendicular to the magnetization direction, respectively. Here (even) and (odd) denote the even and odd parts with respect to the permutation of the spin basis, which corresponds to the time-reversal symmetry. Performing the each spherical surface integral in (24), we obtain the spin conductivity tensor in the rotational coordinates,

$$\sigma^{\theta} = \begin{pmatrix} 0 & 0 & \sigma_{\perp}^{(\text{odd})} \\ 0 & 0 & -\sigma_{\perp}^{(\text{even})} \\ \sigma_{\perp}^{(\text{odd})} & -\sigma_{\perp}^{(\text{even})} & 0 \end{pmatrix}, \quad (25a)$$

$$\sigma^{\phi} = \begin{pmatrix} 0 & 0 & \sigma_{\perp}^{(\text{even})} \\ 0 & 0 & \sigma_{\perp}^{(\text{odd})} \\ \sigma_{\perp}^{(\text{even})} & \sigma_{\perp}^{(\text{odd})} & 0 \end{pmatrix}, \quad (25b)$$

$$\sigma^m = 2(\bar{\sigma} + \sigma_{\parallel}^{(\text{odd})}) \begin{pmatrix} 1 & 0 & 0 \\ 0 & 1 & 0 \\ 0 & 0 & 1 \end{pmatrix} + \sigma_{\parallel}^{(\text{odd})} \begin{pmatrix} -1 & 0 & 0 \\ 0 & -1 & 0 \\ 0 & 0 & 1 \end{pmatrix}, \quad (25c)$$

and in the stationary coordinate,

$$\begin{aligned} \sigma_{ij}^n &= \sum_{\mu\nu\lambda} R_{n\lambda} R_{i\mu} R_{j\nu} \sigma_{\mu\nu}^{\lambda} \\ &= \sigma_{\perp}^{(\text{odd})} \{R_{jm}(R_{i\theta}R_{n\theta} + R_{i\phi}R_{n\phi}) + R_{im}(R_{n\theta}R_{j\theta} + R_{n\phi}R_{j\phi})\} + \sigma_{\perp}^{(\text{even})} \{R_{jm}(R_{i\theta}R_{n\phi} - R_{i\phi}R_{n\theta}) + R_{im}(R_{n\phi}R_{j\theta} - R_{n\theta}R_{j\phi})\} \\ &\quad + R_{nm} \{2(\bar{\sigma} + \sigma_{\parallel}^{(\text{odd})})\delta_{j,i} + \sigma_{\parallel}^{(\text{odd})} (R_{jm}R_{im} - R_{j\theta}R_{i\theta} - R_{j\phi}R_{i\phi})\}. \end{aligned} \quad (26)$$

When $\hat{\mathbf{m}} = (0, 0, 1)$, both $\sigma_{\mu\nu}^{\lambda}$ and σ_{ij}^n are identical. Moreover, the spin conductivity tensor on the stationary coordinate for the field and current direction and the rotational coordinate for spin polarization is

$$\sigma_{ij}^{\theta} = \sigma_{\perp}^{(\text{odd})} (R_{im}R_{j\theta} + R_{jm}R_{i\theta}) - \sigma_{\perp}^{(\text{even})} (R_{im}R_{j\phi} + R_{jm}R_{i\phi}), \quad (27a)$$

$$\sigma_{ij}^{\phi} = \sigma_{\perp}^{(\text{odd})} (R_{im}R_{j\phi} + R_{jm}R_{i\phi}) + \sigma_{\perp}^{(\text{even})} (R_{im}R_{j\theta} + R_{jm}R_{i\theta}), \quad (27b)$$

$$\sigma_{ij}^m = 2(\bar{\sigma} + \sigma_{\parallel}^{(\text{odd})})\delta_{i,j} + \sigma_{\parallel}^{(\text{odd})} (R_{im}R_{jm} - R_{i\theta}R_{j\theta} - R_{i\phi}R_{j\phi}), \quad (27c)$$

with the same rotation matrix R as Eq. (2). For example, in the case of Eq. (27), the transverse spin conductivity with $i = y$, $j = x$ when $\theta_m = \frac{\pi}{2}$ is

$$\sigma_{yx}^{\theta} = \sigma_{\perp}^{(\text{even})} \cos 2\phi_m, \quad (28a)$$

$$\sigma_{yx}^{\phi} = -\sigma_{\perp}^{(\text{odd})} \cos 2\phi_m, \quad (28b)$$

$$\sigma_{yx}^m = \sigma_{\parallel}^{(\text{odd})} \sin 2\phi_m. \quad (28c)$$

In Appendix A, we provide some more examples of spin conductivity tensor in the stationary coordinate system. Note that Eqs. (25)–(27) hold for any system as long as the nonperturbative Green's function \tilde{C}_0 is isotropic in the momentum space. The details of the electronic state are imposed on the coefficients $\sigma_{\perp}^{(\text{odd})}$, $\sigma_{\perp}^{(\text{even})}$, and $\sigma_{\parallel}^{(\text{odd})}$. σ_{ij}^m in Eq. (27c) represents the spin-conduction polarized parallel to the magnetization. This corresponds to the PHE-SC in the two-current model limit, which treats each spin band independently when spin band mixing is sufficiently small [11]. In contrast to σ_{ij}^m , σ_{ij}^{θ} and σ_{ij}^{ϕ} in Eqs. (27a) and (27b) represent the spin conduction polarized along a direction perpendicular to the magnetization.

Here, we comment on the shape of the tensor in Eq. (25) in terms of symmetry. The symmetry constraints on the spin conductivity tensor have been established [26,27]. Because our model does not include any lattice ($\Delta_C = \Delta_T = 0$ in this section), its symmetry is the same as that of a ferromagnetic electron gas. In such case, the symmetry-constrained spin conductivity tensor is obtained as

$$\sigma^{\theta} = \begin{pmatrix} 0 & 0 & x_{002} \\ 0 & 0 & -x_{102} \\ x_{020} & -x_{120} & 0 \end{pmatrix}, \quad \sigma^{\phi} = \begin{pmatrix} 0 & 0 & x_{102} \\ 0 & 0 & x_{002} \\ x_{120} & x_{020} & 0 \end{pmatrix}, \quad \sigma^m = \begin{pmatrix} x_{200} & -x_{210} & 0 \\ x_{210} & x_{200} & 0 \\ 0 & 0 & x_{222} \end{pmatrix}, \quad (29)$$

by using the Symmetr code [47]. Thus, the tensor form in Eq. (25) is permitted in terms of symmetry. The tensor in Eq. (29) can be found in all magnetic Laue groups which are compatible with ferromagnetism because an electron gas has higher symmetry than any other lattices [48]. The individual tensors in Eq. (25) are symmetric under a permutation of field and current direction whereas the general tensors in Eq. (29) do not have to be symmetric, for example, $x_{020} \neq x_{002}$. Note that while the ASF scattering mechanism only produces the symmetric contribution in this work, a symmetric tensor is not necessarily a signature of this

mechanism. Other microscopic origins can also contribute to symmetric tensors, and they are generally not distinguishable by macroscopic symmetry.

We next derive the coefficients in Eq. (24), expressed as

$$\sigma_{\perp}^{(\text{odd})} = -\frac{15}{4\pi^3} n_{\text{imp}} e \left(\frac{\lambda \hbar^2}{m} \right)^2 \int_0^{\infty} dk k^4 \text{Re} V_{\uparrow} V_{\downarrow} \Upsilon_{\uparrow}^+ \Upsilon_{\downarrow}^+ G_{0,\uparrow}^+ G_{0,\downarrow}^+ (G_{0,\uparrow}^- + G_{0,\downarrow}^-) + (\dots), \quad (30a)$$

$$\sigma_{\perp}^{(\text{even})} = -\frac{15}{4\pi^3} n_{\text{imp}} e \left(\frac{\lambda \hbar^2}{m} \right)^2 \int_0^{\infty} dk k^4 \text{Im} V_{\uparrow} V_{\downarrow} \Upsilon_{\uparrow}^+ \Upsilon_{\downarrow}^+ G_{0,\uparrow}^+ G_{0,\downarrow}^+ (G_{0,\uparrow}^- - G_{0,\downarrow}^-) + (\dots), \quad (30b)$$

$$\sigma_{\parallel}^{(\text{odd})} = -\frac{15}{4\pi^3} n_{\text{imp}} e \left(\frac{\lambda \hbar^2}{m} \right)^2 \int_0^{\infty} dk k^4 \text{Re} (\Upsilon_{\uparrow}^+ - \Upsilon_{\downarrow}^+) \{ V_{\uparrow}^2 (\Upsilon_{\uparrow}^+)^2 G_{0,\uparrow}^+ (G_{0,\uparrow}^-)^2 - V_{\downarrow}^2 (\Upsilon_{\downarrow}^+)^2 G_{0,\downarrow}^+ (G_{0,\downarrow}^-)^2 \} + (\dots), \quad (30c)$$

where $G_{0,\sigma}^{\pm} = [\tilde{G}_0]_{\sigma,\sigma}$ and (\dots) denote the terms including $(G_{0,\sigma}^{\pm})^3$, whose contribution can be neglected in a diffusive metal region. Because we consider dissipative conduction in metallic bands, we can neglect (\dots) in Eq. (30). Assuming $\eta_{\text{ss}} = \frac{\hbar}{2\tau_0} \ll E_{\text{F}}$ and using the relations $G_{0,\sigma}^+(k)G_{0,\sigma}^-(k) \simeq \frac{2\pi\tau_0}{\hbar} \delta(E_{\text{F}} - E_{k\sigma})$, $G_{0,\sigma}^+(k_{\text{F}\sigma}) \simeq -i\frac{\tau_0}{\hbar}$, and $G_{0,\sigma}^+(k_{\text{F}\bar{\sigma}}) \simeq \sigma \frac{1}{2\Delta_s}$ with Fermi momentum of spin- σ band, $k_{\text{F}\sigma}$, we can derive

$$\sigma_{\perp}^{(\text{odd})} \simeq -\frac{\hbar}{2e} \frac{3n_{\text{imp}}\lambda^2}{8(E_{\uparrow} - E_{\downarrow})} \{ \sigma_{\uparrow} V_{\uparrow}(k_{\text{F}\downarrow}) V_{\downarrow}(k_{\text{F}\downarrow}) - \sigma_{\downarrow} V_{\uparrow}(k_{\text{F}\uparrow}) V_{\downarrow}(k_{\text{F}\uparrow}) \} \text{Re}[(\Upsilon_{\uparrow}^+ - \Upsilon_{\downarrow}^+) \Upsilon_{\uparrow}^+ \Upsilon_{\downarrow}^+], \quad (31a)$$

$$\sigma_{\perp}^{(\text{even})} \simeq \frac{\hbar}{2e} \frac{3n_{\text{imp}}\lambda^2}{8\pi(E_{\uparrow} - E_{\downarrow})} \{ \sigma_{\uparrow} V_{\uparrow}(k_{\text{F}\downarrow}) V_{\downarrow}(k_{\text{F}\downarrow}) + \sigma_{\downarrow} V_{\uparrow}(k_{\text{F}\uparrow}) V_{\downarrow}(k_{\text{F}\uparrow}) \} \text{Im}[(\Upsilon_{\uparrow}^+ - \Upsilon_{\downarrow}^+) \Upsilon_{\uparrow}^+ \Upsilon_{\downarrow}^+], \quad (31b)$$

$$\sigma_{\parallel}^{(\text{odd})} \simeq -\frac{3n_{\text{imp}}\lambda^2}{2e} \{ \sigma_{\uparrow} \tau_{\uparrow} V_{\uparrow}^2(k_{\text{F}\uparrow}) \text{Im}[(\Upsilon_{\uparrow}^+ - \Upsilon_{\downarrow}^+) (\Upsilon_{\uparrow}^+)^2] + \sigma_{\downarrow} \tau_{\downarrow} V_{\downarrow}^2(k_{\text{F}\downarrow}) \text{Im}[(\Upsilon_{\uparrow}^+ - \Upsilon_{\downarrow}^+) (\Upsilon_{\downarrow}^+)^2] \}, \quad (31c)$$

where $\sigma_{\sigma} \equiv e^2 n_{\sigma} \tau_0 / m$ represents the nonperturbative conductivity of the spin- σ band with the Fermi momentum $k_{\text{F}\sigma}$ and the carrier concentration of the Fermi gas $n_{\sigma} = \frac{k_{\text{F}\sigma}^3}{6\pi^2}$. Because all the expressions have $(\Upsilon_{\uparrow}^+ - \Upsilon_{\downarrow}^+)$, these terms never appear for a nonmagnetic impurity. From Eq. (31), we can obtain a scaling law for the spin Hall (magnetic spin Hall) resistivity $\rho^{\text{SHE}(\text{MSHE})} \equiv \sigma_{\perp}^{\text{even}(\text{odd})} / (\sigma_{\uparrow} + \sigma_{\downarrow})^2$ with respect to the longitudinal charge resistivity ρ_{xx} as

$$\rho^{\text{SHE}} \propto \rho_{xx}, \quad \rho^{\text{MSHE}} \propto P(E_{\text{F}}) \rho_{xx}, \quad (32)$$

where $P(E_{\text{F}}) \equiv (\sigma_{\uparrow} - \sigma_{\downarrow}) / (\sigma_{\uparrow} + \sigma_{\downarrow})$ is the spin-polarization ratio at the Fermi energy. Both ρ^{SHE} and ρ^{MSHE} scale linearly with respect to ρ_{xx} , which is the same as the skew-scattering mechanism of the conventional SHE.

We finally discuss how spin-dependent scattering with the SOI produces a transverse spin conduction. To determine the microscopic mechanism of both $\sigma_{\perp}^{(\text{even})}$ and $\sigma_{\perp}^{(\text{odd})}$, we analyzed the elementary processes of scattering, as shown in Fig. 6. Here, we define the ladder operators $\tilde{\sigma}_{\pm} = (\tilde{\sigma}_{\theta} \pm i\tilde{\sigma}_{\phi})/2$. This process is referred to as anisotropic spin-flip (ASF) scattering, highlighting its two distinctive features: spin flipping and anisotropic (\hat{k} -dependent) hybridization strength. In ASF, the electrons are observed as the spin current of $\tilde{\sigma}_{\pm}$ after experiencing s - d hybridization and propagation in the d state with the SOI. The SOI plays two important roles in ASF as orbital splitting ($l_m \tilde{\sigma}_m$) and orbital elevation with spin flipping ($l_{\pm} \tilde{\sigma}_{\mp}$). The spin flipping leads to a perpendicular-polarized spin current, which includes both the T-even term and the T-odd term, as shown in Eqs. (25b) and (25a). Moreover, because of the orbital elevation, the incoming and outgoing d -orbital states can be different, such as $\tilde{V}_M^{\text{sd}} \tilde{V}_{M' \neq M}^{\text{ds}}$. Because $\tilde{V}^{\text{sd}} \propto Y_{2,M}(\hat{k})$ has an M -dependent

anisotropic shape, a mixture of \tilde{V}_M^{sd} and $\tilde{V}_{M' \neq M}^{\text{ds}}$ is required for the spin conductivity to have not only the longitudinal component (σ_{ii}^{μ}), but also the transverse component (σ_{ij}^{μ}). The orbital splitting l_m is required to avoid the cancellation of $\tilde{V}_M^{\text{sd}} \tilde{V}_{M\pm 1}^{\text{ds}}$ and $\tilde{V}_{-M}^{\text{sd}} \tilde{V}_{-(M\pm 1)}^{\text{ds}}$; therefore, the ASF-SHE/MSHE should be obtained from the second- or higher-order perturbation with respect to the SOI. For example, when the incoming state $M = 0$ and outgoing state $M' = +1$, the transverse spin-current contribution $\sigma_{\theta m}^{\theta(\phi)}$ can be obtained as

$$\sigma_{\theta m}^{\theta(\phi)} \propto \int d\mathbf{k} \hat{k}_m \hat{k}_{\theta(\phi)} (3\hat{k}_m^2 - 1) \{ \hat{k}_m (\hat{k}_{\theta} + i\hat{k}_{\phi}) \} \neq 0. \quad (33)$$

B. Kinetic view of the anisotropic spin-flip scattering

To provide an intuitive understanding of both ASF-SHE and ASF-MSHE, we constructed a kinetic view of these phenomena using the equations of motion based on the Boltz-

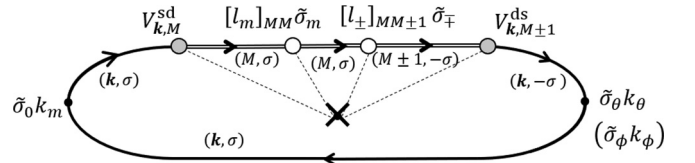


FIG. 6. Diagrammatic representation of an s - d scattering process contributing both to the magnetic and the spin Hall effect, which corresponds directly to Fig. 1(b). The solid and double lines represent the electrons of the conduction bands and impurity d -orbital states, respectively. The gray points represent s - d hybridization, and the white point represents the spin-orbit interaction on the d -orbital states.

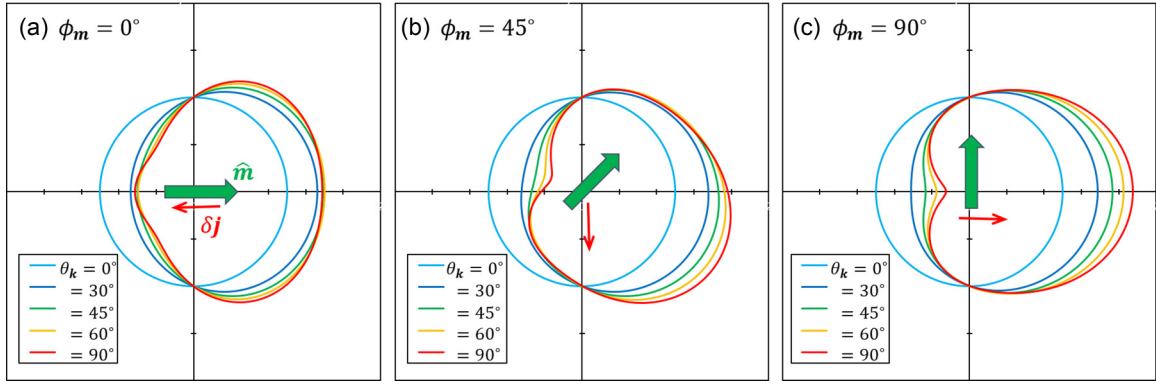


FIG. 7. Polar plot for the nonequilibrium charge distribution function f_0 with respect to ϕ_k for the different magnetization directions: (a) $\phi_m = 0^\circ$, (b) $\phi_m = 45^\circ$, and (c) $\phi_m = 90^\circ$, where ϕ_k and ϕ_m are the azimuthal angles of $\hat{\mathbf{k}}$ and $\hat{\mathbf{m}}$ on the stationary coordinate system. Each line corresponds to the projection of θ_k and the polar angle of $\hat{\mathbf{k}}$. The bold arrow represents $\hat{\mathbf{m}}$, and the thin red arrow represents the anisotropic part of the charge current induced by the direction-dependent distribution.

mann transport theory in the spin or space. We define the 2×2 matrix of the nonequilibrium electron distribution function as

$$\tilde{f}(\mathbf{k}) = \tilde{\sigma}_0 f_0(\mathbf{k}) + \hat{\sigma} \cdot \mathbf{f}(\mathbf{k}), \quad (34)$$

where f_0 is the charge distribution, and f_μ is the spin distribution with spin $\mu = \theta, \phi, m$. We assume a three-dimensional ferromagnetic electron gas with a weak SOI, which leads to a spin-diagonal equilibrium distribution function with $f_{\text{eq},\uparrow}$ and $f_{\text{eq},\downarrow}$, and start with the Boltzmann equation for a steady state

with the relaxation time approximation [49]

$$-\frac{eE_x v_x}{\hbar} \tilde{f}'(\mathbf{k}) = -\frac{1}{2} \{\tilde{\tau}^{-1}, \delta \tilde{f}(\mathbf{k})\}, \quad (35)$$

with $\tilde{f}'(\mathbf{k}) = \partial \tilde{f}(\mathbf{k}) / \partial \varepsilon_{\uparrow, \mathbf{k}} = \partial \tilde{f}(\mathbf{k}) / \partial \varepsilon_{\downarrow, \mathbf{k}}$. $\delta \tilde{f}(\mathbf{k}) = \tilde{f}(\mathbf{k}) - \tilde{f}_{\text{eq}}(\mathbf{k})$ denotes the deviation from the equilibrium distribution. The relaxation time $\tilde{\tau}$ is spin-dependent and is represented by a 2×2 matrix. Hereinafter, we assume the ϕ scan ($\theta_m = \pi/2$) for the magnetization direction until the end of this section. Using the results of Eqs. (14) and (15), we define a relaxation time which depends on the momentum direction (θ_k, ϕ_k) as well as the magnetization direction ϕ_m , and obtain a linear response solution of Eq. (35):

$$\delta f_0(\mathbf{k}) \propto \{h_0 + [f'_{\text{eq},\uparrow}(\mathbf{k}) - f'_{\text{eq},\downarrow}(\mathbf{k})] \sin^2 \theta_k \cos^2(\phi_k - \phi_m)\} \sin \theta_k \cos \phi_k, \quad (36a)$$

$$\delta f_m(\mathbf{k}) \propto \{h_z + [f'_{\text{eq},\uparrow}(\mathbf{k}) + f'_{\text{eq},\downarrow}(\mathbf{k})] \sin^2 \theta_k \cos^2(\phi_k - \phi_m)\} \sin \theta_k \cos \phi_k, \quad (36b)$$

$$\delta f_\theta(\mathbf{k}) \propto [f'_{\text{eq},\uparrow}(\mathbf{k}) + f'_{\text{eq},\downarrow}(\mathbf{k})] \sin^2 \theta_k \sin 2(\phi_k - \phi_m) \sin \theta_k \cos \phi_k, \quad (36c)$$

$$\delta f_\phi(\mathbf{k}) \propto [f'_{\text{eq},\uparrow}(\mathbf{k}) - f'_{\text{eq},\downarrow}(\mathbf{k})] \sin^2 \theta_k \sin 2(\phi_k - \phi_m) \sin \theta_k \cos \phi_k, \quad (36d)$$

where the terms h_0 and h_z are independent of $\hat{\mathbf{k}}$ and $\hat{\mathbf{m}}$, respectively. The derivation is given in Appendix B. First, we observe the momentum dependence of the charge distribution, $f_0(\mathbf{k})$, as plotted in Figs. 7(a)–7(c). Reflecting the s - d scattering nature of the relaxation time, $\delta f_0(\mathbf{k})$ shows an anisotropic distribution depending on the relative angle between the magnetization angle ϕ_m and momentum angle ϕ_k . Comparing $\phi_m = 0$ and $\phi_m = \frac{\pi}{2}$ in Fig. 7, the distribution along the x axis is different, and therefore the longitudinal current j_x^0 is modulated by the direction of magnetization. This behavior can be understood as the AMR effect. For $\phi_m = \frac{\pi}{4}$, the distribution is biased in the y -axis direction and provides finite transverse currents j_y^0 , which is the PHE.

Similarly, $\delta f_\theta(\mathbf{k})$ and $\delta f_\phi(\mathbf{k})$ also have momentum-dependent distributions as shown in Figs. 8(a)–8(c), resulting in nonequilibrium spin currents polarized along $\hat{\theta}$ or $\hat{\phi}$. When $\phi_m = 0$ or $\phi_m = \frac{\pi}{2}$, as shown in Fig. 8, the finite transverse spin currents j_y^θ, j_y^ϕ , which correspond to ASF-SHE/MSHE, exist. Namely, the ASF-SHE/MSHE can be understood intu-

tively in a similar way to the PHE in terms of the anisotropic spin-dependent relaxation time. The ASF-SHE/MSHE is governed by spin-flip scattering, whereas the PHE is governed by spin-dependent momentum scattering. When $\phi_m = \frac{\pi}{4}$, there are finite longitudinal spin currents j_x^θ, j_x^ϕ , which can be understood similarly to the AMR effect.

Note that a nonequilibrium anisotropic spin distribution of this nature is not specific to the momentum- and magnetization-dependent relaxation time, as discussed here. When the Fermi surface has spin-momentum locking, a constant relaxation time can also generate a spin distribution and a resultant spin current, which can show the same magnetization dependence [21]. Although both mechanisms can contribute to the spin current with the same symmetry, they show quantitatively different dependencies on parameters, reflecting their different microscopic origins. Therefore, we would obtain both contributions and their interference effect if we were to utilize both the spin-momentum locking Fermi surface and magnetization-dependent relaxation time.

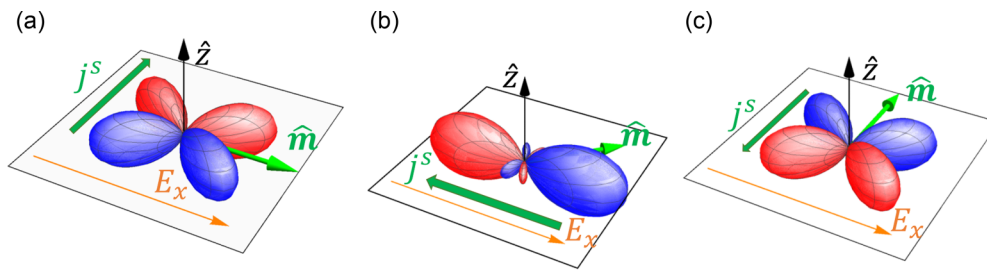


FIG. 8. Spherical plot for the isosurface of a nonequilibrium spin distribution function δf_θ with respect to ϕ_k for the different magnetization directions: (a) $\phi_m = 0^\circ$, (b) $\phi_m = 45^\circ$, and (c) $\phi_m = 90^\circ$. The colored area represents the sign of the distribution function, with red and blue denoting positive and negative signs, respectively. The \uparrow spins are more likely to flip to \downarrow for the red area, and vice versa for the blue area, which corresponds to the illustration in Fig. 1. Note that δf_ϕ shows the same isosurface as δf_θ .

C. Numerical calculation

We numerically evaluated Eq. (20) to test the validity of the perturbative analysis developed in the previous section and qualitatively investigate the dependence on several parameters including the crystal-field splitting. In this section, we focus on σ_{yx}^μ with $\mu = \theta, \phi, m$. We set the parameters $\Delta_s = \Delta_d = 0.5$ and $\xi = -0.025$ in units of $\hbar^2/2m$, which we consider to be reasonable for ferromagnetic metals. We take the bottom of the conduction electron band as the reference point for the energy and set $E_{\text{imp}} = 0.45$. The density of states (DOS) is shown in Fig. 9. For simplicity, we assume $V_\uparrow(k_F) = V_\downarrow(k_F) = V$, and choose the parameters related to impurity scattering as $n_{\text{imp}}V^2 = 0.1$ and $\eta_{ss} = \eta_d = 0.1$.

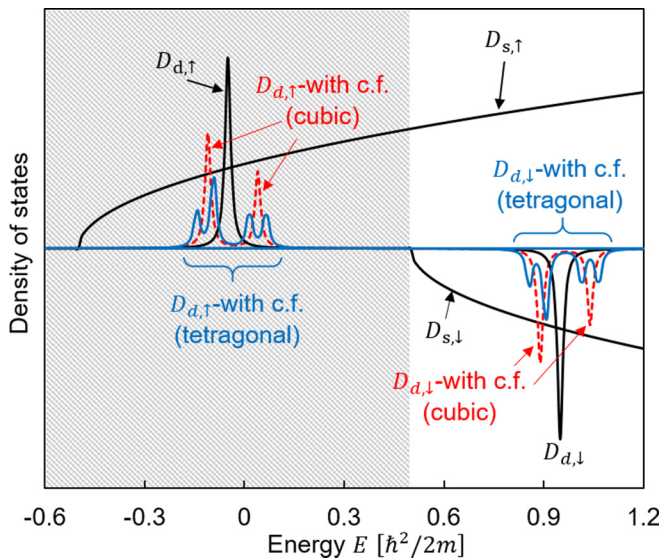


FIG. 9. Schematics of the projected density of states (PDOS) of the conduction bands and the 3d level for $E_{\text{imp}} = 0.45$ and $\Delta_s = \Delta_d = 0.5$. The solid gray and solid black lines represent the PDOS of the conduction band and the PDOS of the 3d states for each spin, respectively. The dotted red and blue lines represent the PDOS of each splitting 3d level due to the cubic and tetragonal crystal fields, respectively. The hatched area represents a half-metallic region, where a single spin conduction band is present. To improve visualization, the spin-orbit interaction is ignored, and the spectral widths are adjusted using different values from those in the numerical calculations.

First, we show the dependence of the spin conductivities on the direction of magnetization and Fermi energy in the case of $\Delta_C = \Delta_T = 0$, and then compare the results of the perturbative analysis. Hereinafter, we consider the spin Hall angles (SHAs) $\vartheta_{yx}^\mu \equiv -\frac{\hbar}{2e} \sigma_{yx}^\mu / \sigma_{xx}^0$ instead of σ_{yx}^μ . Figure 10 shows the dependencies of the SHAs on the magnetization angle in the ϕ scan ($\theta_m = \pi/2$) with $E_F = 0.9$. These results are consistent with the prediction of the perturbative analysis in Eq. (28) because we find that the $\sigma_{yx}^\theta, \sigma_{yx}^\phi \propto \cos 2\phi$ and $\sigma_{yx}^m \propto \sin 2\phi$. The Fermi energy dependencies of $\vartheta_\perp^{\text{(even)}}$, $\vartheta_\perp^{\text{(odd)}}$, $\vartheta_\parallel^{\text{(odd)}}$ and the planar Hall angle (PHA) are shown in Figs. 11(a) and 11(b). The results show that all of the plots have peaks because of resonant scattering in the vicinity of each impurity level. Referring to Eq. (31), it is clear that these resonance peaks reflect the spectral structure of the Green's functions of each of the d -orbital states. In panel (a), the PHA takes values of approximately $\lesssim 2\%$, which seems of a reasonable order of magnitude in a typical ferromagnetic metal, although we use a simplified model with roughly estimated parameters. In the half-metallic region ($E_F \lesssim 0.55$), $\sigma_\parallel^{\text{(odd)}}$ is roughly proportional to the PHA, supporting the spin-polarized PHE. In the normal metallic region ($E_F \gtrsim 0.55$), the relationship between $\vartheta_\parallel^{\text{(odd)}}$ and PHA becomes more complex because the contribution from both spin bands is tangled. $\vartheta_\parallel^{\text{(odd)}}$ tends to be enhanced in the half-metal region rather than in the normal

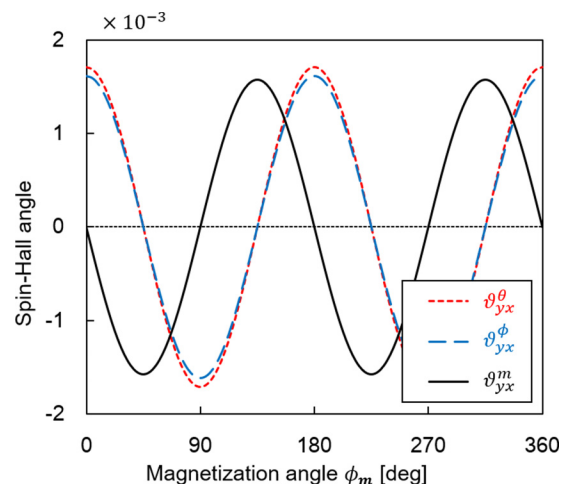


FIG. 10. Spin Hall angles $\vartheta_{yx}^\mu \equiv -(2e/\hbar)\sigma_{yx}^\mu/\sigma_{xx}^0$ as functions of the in-plane magnetization direction ϕ_m .

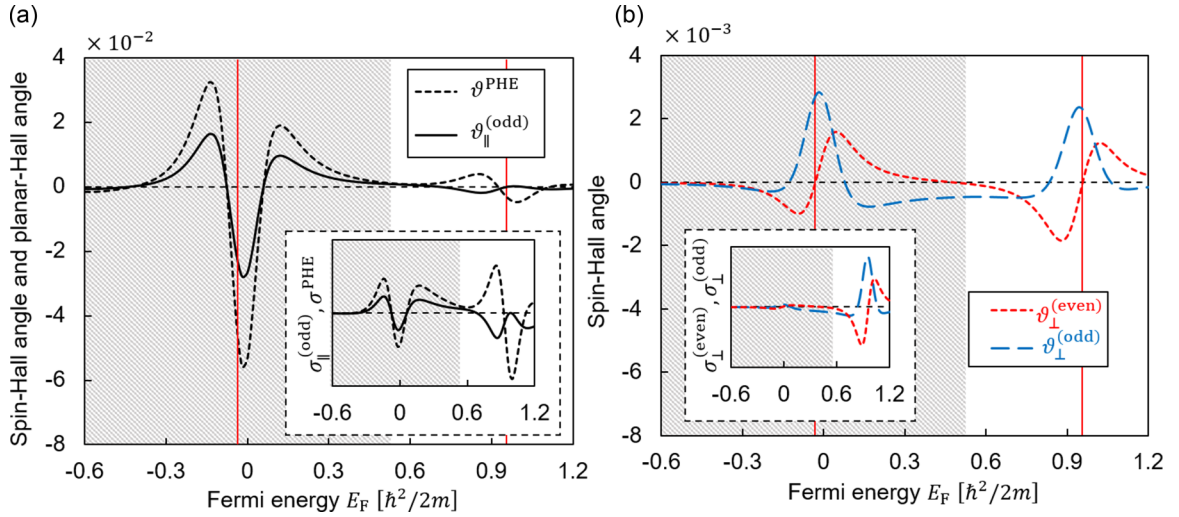


FIG. 11. Fermi energy dependencies of the spin Hall angles for (a) $\sigma_{\parallel}^{(\text{odd})}$ and (b) $\sigma_{\perp}^{(\text{even})}$, $\sigma_{\perp}^{(\text{odd})}$. The vertical red line represents the position of each $3d$ level. The insets show the intensities of each spin conductivity before being normalized by the longitudinal conductivity. The planar Hall angle is also plotted in (a). The hatched area represents the half-metallic region shown in Fig. 9.

metallic region. This is because σ_{xx} in the half-metal region is smaller than that in the normal metal region. In contrast, $\sigma_{\parallel}^{(\text{odd})}$ maintains the same order of magnitude from the half-metal region to the normal metal region. On the other hand, in panel (b), because $\vartheta_{\perp}^{(\text{even})}$ and $\vartheta_{\perp}^{(\text{odd})}$ are governed by the mixing of Υ_{\uparrow} and Υ_{\downarrow} , little difference in magnitude exists between the half-metallic and normal metallic regions. Note that this is the case for the SHA; however, the absolute value of the spin conductivity itself increases with increasing longitudinal conductivity, as shown in the inset of Fig. 11(b). Comparing the behavior of $\vartheta_{\perp}^{(\text{even})}$ and $\vartheta_{\perp}^{(\text{odd})}$ with Eqs. (31b) and (31a), it becomes possible to obtain the characteristics of the real and the imaginary parts of the Green's function.

Next, we present the calculation results by taking into account the cubic or tetragonal crystal field, either of which splits the $3d$ -orbital states, as shown in Fig. 9. Figures 12(a) and 12(b) show the magnetization angular dependencies of SHAs under the cubic field ($\Delta_C = 0.15$, $\Delta_T = 0$) and the

tetragonal field ($\Delta_C \neq 0$, $\Delta_T \neq 0$). Compared to the results obtained without the crystal field (Fig. 10), the crystal fields change not only the angular dependency but the amplitudes in each component of the SHA.

Figure 13 shows the Fermi energy dependencies of $\vartheta_{\perp}^{(\text{even})}$ and $\vartheta_{\perp}^{(\text{odd})}$ for various values of the cubic field. In both results, the resonance peaks shift together with the splitting $3d$ levels when $\Delta_C \neq 0$, whereas the behavior around each peak is similar to that in the case of $\Delta_C = 0$. This trend also holds for the tetragonal crystal field. Figure 14 shows the Fermi energy dependencies of $\vartheta_{\perp}^{(\text{even})}$ and $\vartheta_{\perp}^{(\text{odd})}$ for various values of the tetragonal field. Similarly to Fig. 13, the peaks shift together with the $3d$ levels without any drastic change of the functions. These results suggest that the cubic or tetragonal crystal field can modify the magnitude of the SHAs via the splitting of the $3d$ states, but do not change the physical view of $\vartheta_{\perp}^{(\text{even})}$ and $\vartheta_{\perp}^{(\text{odd})}$ that arise from the s - d scattering with anisotropic spin flipping. Therefore, we expect both the ASF-SHE and

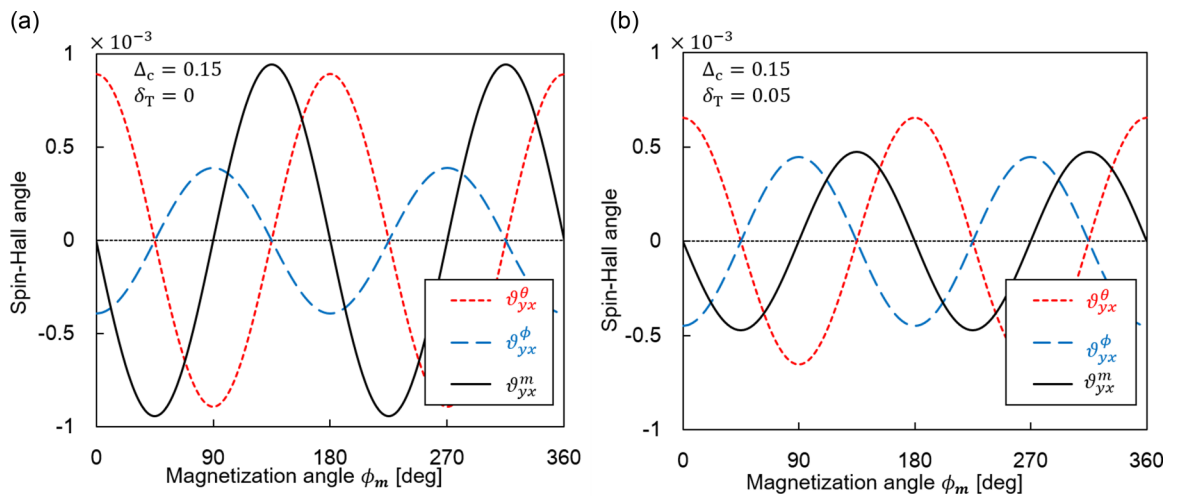


FIG. 12. Spin Hall angles $\tilde{\sigma}_{yx}^{\mu} \equiv -(2e/\hbar)\sigma_{yx}^{\mu}/\sigma_{xx}^0$ as functions of the in-plane magnetization direction ϕ_m with (a) the cubic field splitting $\Delta_C = 0.15$, $\Delta_T = 0.0$ and (b) the tetragonal field splitting $\Delta_C = 0.15$, $\Delta_T = 0.05$.

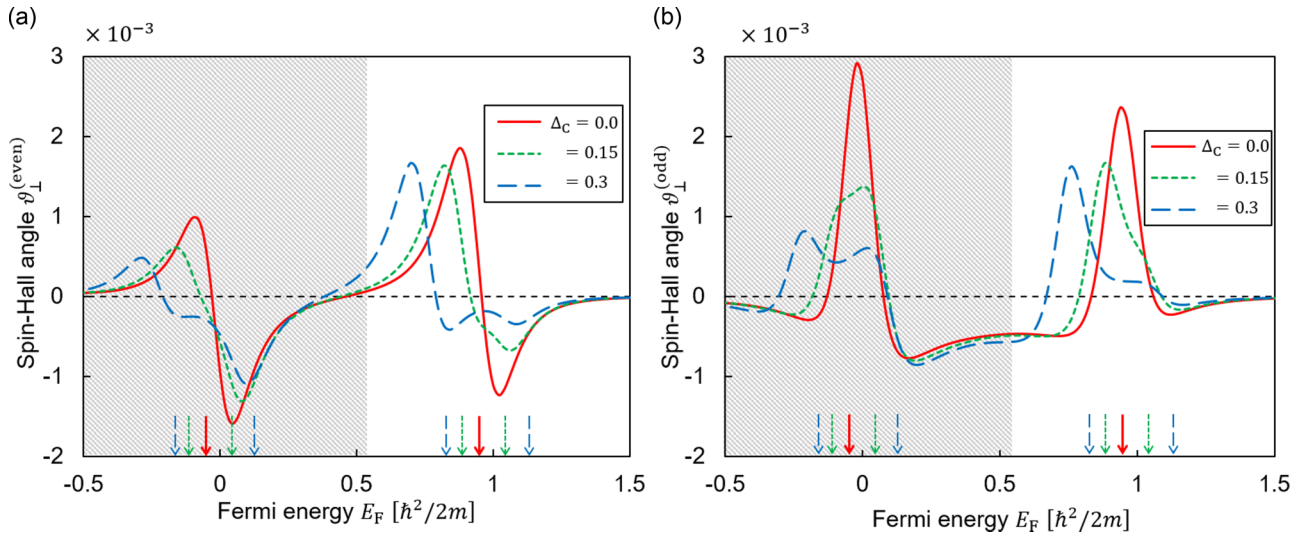


FIG. 13. Fermi energy dependencies of spin Hall angles for (a) $\sigma_{\perp}^{(\text{even})}$ and (b) $\sigma_{\perp}^{(\text{odd})}$ for various values of the cubic crystal field $\Delta_C = 0.0, 0.15, 0.3$. The arrows at the bottom represent the positions of the corresponding energy levels.

ASF-MSHE to be robust against the crystal field effect and to appear in actual materials.

IV. SUMMARY

We proposed an extrinsic mechanism for the spin Hall effect (SHE), which arises from anisotropic spin flipping in the electron scattering processes. We assumed the existence of s - d scattering in a ferromagnetic $3d$ alloy and represented it using a multiorbital impurity Anderson model considering the spin-orbit interaction (SOI) and the crystal-field splitting of the d -orbital states. The spin conductivities were formulated using microscopic transport theory based on the Kubo formula within the averaged T -matrix approximation for randomness. To determine the physical aspect of the spin conductivity, we first performed an analytical derivation using a perturbation expansion with respect to the SOI up to the second order. As a result, we obtained the spin conductivity tensor with both contributions to the time-reversal even (SHE) and the time-

reversal odd (magnetic SHE) from the anisotropic spin-flip scattering (ASF) process: a scattering process that combines the anisotropic (spatially dependent) s - d hybridization and spin flip by the SOI. From a microscopic viewpoint, the ASF can be understood as the coupling between the momentum of the s electron and its spin via the intermediate d orbital of an impurity, which is a result of the combination of the SOI in the d orbital and the orbital-selective s - d transition. The spin current of both effects follows $\cos 2\phi$, where ϕ is the relative angle between the magnetization and the applied electric field, and their spin Hall resistivities approximately scale linearly with the longitudinal resistivity in the diffusive metal region. For the analytical calculation, we disregarded the crystal-field splitting for simplicity. In the kinetic view, the ASF scattering processes are responsible for a ϕ -dependent spin-flip relaxation time, which induces an anisotropic nonequilibrium spin distribution and consequently generates a finite spin current. This is similar to the planar Hall effect (PHE) in bulk ferromagnets, which arises from an anisotropic nonequilibrium

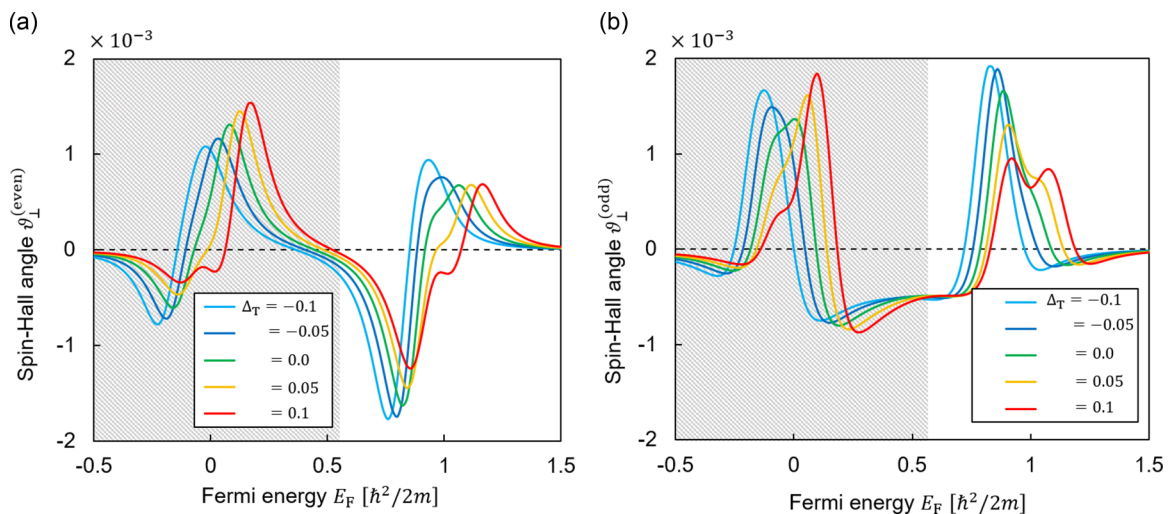


FIG. 14. Fermi energy dependencies of spin Hall angles for (a) $\sigma_{\perp}^{(\text{even})}$ and (b) $\sigma_{\perp}^{(\text{odd})}$ for various values of the tetragonal distortion $\Delta_T = -0.1, -0.05, 0.0, 0.05, 0.1$ and the cubic crystal field $\Delta_C = 0.15$ (fixed).

charge distribution. A distinctive feature of the ASF-SHE is that the spin current is polarized perpendicular to \hat{m} and controllable by the magnetization direction. We also performed numerical calculations to determine the influence of the crystal-field splitting. The ϕ dependencies and Fermi energy dependencies were computed for different strengths of the crystal field. As a result of their dependencies on ϕ , both the spin Hall angle (SHA) of the ASF-SHE and the ASF-MSHE were proportional to $\cos 2\phi$, in agreement with the perturbative results even with cubic or tetragonal crystal fields. From the Fermi energy dependencies, we found that the crystal fields appear to produce only energy shifts owing to the level splitting among d states and do not suppress the spin current. The results suggest that both the ASF-SHE and ASF-MSHE are robust against orbital splitting owing to the crystal fields; therefore, they can appear in actual materials. Although both the ASF-SHE and ASF-MSHE have not yet been experimentally determined, we expect that a contribution from these effects can be involved in the SHE signals of precursive measurements in ferromagnetic metals. If they occur, we expect their contribution to show linear scaling with the longitudinal charge conductivity and a twofold ($\cos 2\phi$) dependence with respect to the relative angle between the applied electric field and the magnetization direction.

ACKNOWLEDGMENTS

This study was supported by the Center for Spintronics Research Network (CSRN). Y.Y. acknowledges support from GP-Spin at Tohoku University. J.Ž. acknowledges the Grant Agency of the Czech Republic Grant No. 19-18623Y, Ministry of Education of the Czech Republic Grants No. LM2018110, No. LNSM-LNSpin, EU FET Open RIA Grant No. 766566, and support from the Institute of Physics of the Czech Academy of Sciences and the Max Planck Society through the Max Planck Partner Group Programme. This work was supported by the Ministry of Education, Youth and Sports of the Czech Republic through the e-INFRA CZ (ID:90140).

APPENDIX A: MAGNETIZATION ANGULAR DEPENDENCE OF THE SPIN CONDUCTIVITY

To help with practical applications, we provide the magnetization angle θ_m , ϕ_m dependency of the spin conductivity in some specific cases. We firstly derive σ_{xx}^μ and σ_{yx}^μ , ($\mu = \theta, \phi, m$), the longitudinal and transverse spin conductivity with a rotational coordinate spin polarization in Eq. (27), that will be compatible with magnetic resonance measurements.

(i) ϕ_m scan ($\theta_m = \pi/2$, $\phi_m = [0 : 2\pi)$) is

$$\sigma_{xx}^\theta = \sigma_\perp^{(\text{even})} \sin^2 \phi_m, \quad (\text{A1a})$$

$$\sigma_{xx}^\phi = \sigma_\perp^{(\text{odd})} \sin 2\phi_m, \quad (\text{A1b})$$

$$\sigma_{xx}^m = 2(\bar{\sigma} + \sigma_\parallel^{(\text{odd})}) + \sigma_\parallel^{(\text{odd})} \cos 2\phi_m, \quad (\text{A1c})$$

and σ_{yx}^μ is already given in the main text as Eq. (28).

(ii) Polar θ_m scan ($\theta_m = [0 : 2\pi)$, $\phi_m = 0$) is

$$\sigma_{xx}^\theta = \sigma_\perp^{(\text{odd})} \sin^2 \theta_m, \quad (\text{A2a})$$

$$\sigma_{xx}^\phi = \sigma_\perp^{(\text{even})} \sin 2\theta_m, \quad (\text{A2b})$$

$$\sigma_{xx}^m = 2(\bar{\sigma} + \sigma_\parallel^{(\text{odd})}) + \sigma_\parallel^{(\text{odd})} \cos 2\theta_m, \quad (\text{A2c})$$

$$\sigma_{yx}^\theta = -\sigma_\perp^{(\text{even})} \sin \theta_m, \quad (\text{A2d})$$

$$\sigma_{yx}^\phi = \sigma_\perp^{(\text{odd})} \sin \theta_m, \quad (\text{A2e})$$

$$\sigma_{yx}^m = 0. \quad (\text{A2f})$$

(iii) Transverse θ_m scan ($\theta_m = [0 : 2\pi)$, $\phi_m = \pi/2$) is

$$\sigma_{xx}^\theta = 0, \quad (\text{A3a})$$

$$\sigma_{xx}^\phi = 0, \quad (\text{A3b})$$

$$\sigma_{xx}^m = 2\bar{\sigma} + \sigma_\parallel^{(\text{odd})}, \quad (\text{A3c})$$

$$\sigma_{yx}^\theta = \sigma_\perp^{(\text{even})} \sin \theta_m, \quad (\text{A3d})$$

$$\sigma_{yx}^\phi = -\sigma_\perp^{(\text{odd})} \sin \theta_m, \quad (\text{A3e})$$

$$\sigma_{yx}^m = 0. \quad (\text{A3f})$$

We next derive σ_{xx}^n and σ_{yx}^n ($n = x, y, z$), the longitudinal and transverse spin conductivity with a stationary coordinate spin polarization in Eq. (26), which might be convenient to control the spin-polarization direction.

(i) ϕ_m scan ($\theta_m = \pi/2$, $\phi_m = [0 : 2\pi)$) is

$$\sigma_{xx}^x = -\sigma_\perp^{(\text{odd})} \sin 2\phi_m \sin \phi_m + \{2(\bar{\sigma} + \sigma_\parallel^{(\text{odd})}) + \sigma_\parallel^{(\text{odd})} \cos 2\theta_m\} \cos \phi_m, \quad (\text{A4a})$$

$$\sigma_{xx}^y = \sigma_\perp^{(\text{odd})} \sin 2\phi_m \cos \phi_m + \{2(\bar{\sigma} + \sigma_\parallel^{(\text{odd})}) + \sigma_\parallel^{(\text{odd})} \cos 2\theta_m\} \sin \phi_m, \quad (\text{A4b})$$

$$\sigma_{xx}^z = \sigma_\perp^{(\text{even})} \cos 2\phi_m, \quad (\text{A4c})$$

$$\sigma_{yx}^x = \sigma_\perp^{(\text{odd})} \cos 2\phi_m \sin \phi_m + \sigma_\parallel^{(\text{odd})} \sin 2\phi_m \cos \phi_m, \quad (\text{A4d})$$

$$\sigma_{yx}^y = -\sigma_\perp^{(\text{odd})} \cos 2\phi_m \cos \phi_m + \sigma_\parallel^{(\text{odd})} \sin 2\phi_m \cos \phi_m, \quad (\text{A4e})$$

$$\sigma_{yx}^z = -\sigma_\perp^{(\text{even})} \cos 2\phi_m. \quad (\text{A4f})$$

(ii) Polar θ_m scan ($\theta_m = [0 : 2\pi)$, $\phi_m = 0$) is

$$\sigma_{xx}^x = \sigma_\perp^{(\text{odd})} \sin 2\theta_m \cos \theta_m + \{2(\bar{\sigma} + \sigma_\parallel^{(\text{odd})}) + \sigma_\parallel^{(\text{odd})} \cos 2\theta_m\} \sin \theta_m, \quad (\text{A5a})$$

$$\sigma_{xx}^y = \sigma_\perp^{(\text{even})} \sin 2\theta_m, \quad (\text{A5b})$$

$$\sigma_{xx}^z = -\sigma_\perp^{(\text{odd})} \sin 2\theta_m \sin \theta_m + \{2(\bar{\sigma} + \sigma_\parallel^{(\text{odd})}) + \sigma_\parallel^{(\text{odd})} \cos 2\theta_m\} \cos \theta_m, \quad (\text{A5c})$$

$$\sigma_{yx}^x = -\sigma_\perp^{(\text{even})} \sin \theta_m \cos \theta_m, \quad (\text{A5d})$$

$$\sigma_{yx}^y = \sigma_\perp^{(\text{odd})} \sin \theta_m, \quad (\text{A5e})$$

$$\sigma_{yx}^z = \sigma_\perp^{(\text{even})} \sin^2 \theta_m. \quad (\text{A5f})$$

(iii) Transverse θ_m scan ($\theta_m = [0 : 2\pi)$, $\phi_m = \pi/2$) is

$$\sigma_{xx}^x = 0, \quad (\text{A6a})$$

$$\sigma_{xx}^y = (2\bar{\sigma} + \sigma_\parallel^{(\text{odd})}) \sin \theta_m, \quad (\text{A6b})$$

$$\sigma_{xx}^z = (2\bar{\sigma} + \sigma_\parallel^{(\text{odd})}) \cos \theta_m, \quad (\text{A6c})$$

$$\sigma_{yx}^x = \sigma_\perp^{(\text{odd})} \sin \theta_m, \quad (\text{A6d})$$

$$\sigma_{yx}^y = -\sigma_{\perp}^{(\text{even})} \sin \theta_m \cos \theta_m, \quad (\text{A6e})$$

$$\sigma_{yx}^z = -\sigma_{\perp}^{(\text{even})} \sin^2 \theta_m. \quad (\text{A6f})$$

APPENDIX B: NONEQUILIBRIUM SPIN DISTRIBUTION FUNCTION FROM BOLTZMANN EQUATION

In this section, we derive Eq. (36) from Eq. (35). First, we assume the conservation of the spin angular momentum in the stationary state, which means that

$$p_{\uparrow\downarrow} f_{\downarrow\downarrow} + p_{\uparrow\uparrow} f_{\uparrow\downarrow} = f_{\uparrow\uparrow} p_{\uparrow\downarrow} + f_{\uparrow\downarrow} p_{\downarrow\downarrow}, \quad (\text{B1})$$

with

$$\begin{pmatrix} f_{\uparrow\uparrow} & f_{\uparrow\downarrow} \\ f_{\downarrow\uparrow} & f_{\downarrow\downarrow} \end{pmatrix} = \tilde{f}, \quad \begin{pmatrix} p_{\uparrow\uparrow} & p_{\uparrow\downarrow} \\ p_{\downarrow\uparrow} & p_{\downarrow\downarrow} \end{pmatrix} = \tilde{\tau}^{-1}. \quad (\text{B2})$$

The left-hand side of Eq. (B1) represents the probability of gaining $+\frac{\hbar}{2}$ angular momentum on average, whereas the right-hand side represents the probability of losing. When the SOI is sufficiently small, we can ignore the second-order terms of f_{\perp} and p_{\perp} , and Eq. (B1) leads to $[\tilde{p}, \tilde{f}] = \tilde{p}\tilde{f} - \tilde{f}\tilde{p} \simeq 0$. Using this, we can rewrite Eq. (35) to

$$\delta \tilde{f} = \frac{eE_x v_x}{\hbar} \tilde{\tau} \tilde{f}'. \quad (\text{B3})$$

The relaxation time can be derived from $\langle \tilde{T}_{k,k'}(E) \rangle_{\text{conf}}$ given in Eqs. (14) and (15) with Fermi's golden rule,

$$\tilde{\tau}(\hat{\mathbf{k}}, \hat{\mathbf{m}}) = \begin{pmatrix} \bar{\tau}_{\uparrow\uparrow} + \tau'_{\uparrow\uparrow} \sin^2 \theta_k \cos^2(\phi_k - \phi_m) & \tau'_{\uparrow\downarrow} \sin^2 \theta_k \sin 2(\phi_k - \phi_m) \\ \tau'_{\downarrow\uparrow} \sin^2 \theta_k \sin 2(\phi_k - \phi_m) & \bar{\tau}_{\downarrow\downarrow} - \tau'_{\downarrow\downarrow} \sin^2 \theta_k \cos^2(\phi_k - \phi_m) \end{pmatrix}, \quad (\text{B4})$$

where $\tau'_{\sigma\sigma'}$ is the coefficient of the magnetization-dependent terms, and $\bar{\tau}_{\sigma\sigma}$ is the coefficient of the magnetization-independent terms. By substituting this into Eq. (35) and using $v_x \propto k_x \propto \sin \theta_k \cos \phi_k$, we can obtain Eq. (36).

-
- [1] D. Apalkov, B. Dieny, and J. M. Slaughter, *Proc. IEEE* **104**, 1796 (2016).
- [2] S. Bhatti, R. Shibia, A. Hirohata, H. Ohno, S. Fukami, and S. Piramanayagam, *Mater. Today* **20**, 530 (2017).
- [3] S. Ikegawa, F. B. Mancoff, J. Janesky, and S. Aggarwal, *IEEE Trans. Electron Devices* **67**, 1407 (2020).
- [4] J. Sinova, S. O. Valenzuela, J. Wunderlich, C. H. Back, and T. Jungwirth, *Rev. Mod. Phys.* **87**, 1213 (2015).
- [5] P. M. Haney and M. D. Stiles, *Phys. Rev. Lett.* **105**, 126602 (2010).
- [6] B. F. Miao, S. Y. Huang, D. Qu, and C. L. Chien, *Phys. Rev. Lett.* **111**, 066602 (2013).
- [7] B. Zimmermann, K. Chadova, D. Ködderitzsch, S. Blügel, H. Ebert, D. V. Fedorov, N. H. Long, P. Mavropoulos, I. Mertig, Y. Mokrousov *et al.*, *Phys. Rev. B* **90**, 220403(R) (2014).
- [8] D. Tian, Y. Li, D. Qu, S. Y. Huang, X. Jin, and C. L. Chien, *Phys. Rev. B* **94**, 020403(R) (2016).
- [9] A. Davidson, V. P. Amin, W. S. Aljuaid, P. M. Haney, and X. Fan, *Phys. Lett. A* **384**, 126228 (2020).
- [10] G. Qu, K. Nakamura, and M. Hayashi, *Phys. Rev. B* **102**, 144440 (2020).
- [11] T. Taniguchi, J. Grollier, and M. D. Stiles, *Phys. Rev. Appl.* **3**, 044001 (2015).
- [12] C. Qin, S. Chen, Y. Cai, F. Kandaz, and Y. Ji, *Phys. Rev. B* **96**, 134418 (2017).
- [13] K. S. Das, W. Y. Schoemaker, B. J. van Wees, and I. J. Vera-Marun, *Phys. Rev. B* **96**, 220408(R) (2017).
- [14] V. P. Amin, J. Li, M. D. Stiles, and P. M. Haney, *Phys. Rev. B* **99**, 220405(R) (2019).
- [15] T. Seki, S. Iihama, T. Taniguchi, and K. Takanashi, *Phys. Rev. B* **100**, 144427 (2019).
- [16] T. Y. Ma, C. H. Wan, X. Wang, W. L. Yang, C. Y. Guo, C. Fang, M. K. Zhao, J. Dong, Y. Zhang, and X. F. Han, *Phys. Rev. B* **101**, 134417 (2020).
- [17] M. B. Lifshits and M. I. Dyakonov, *Phys. Rev. Lett.* **103**, 186601 (2009).
- [18] C. O. Pauyac, M. Chshiev, A. Manchon, and S. A. Nikolaev, *Phys. Rev. Lett.* **120**, 176802 (2018).
- [19] C. Safranski, E. A. Montoya, and I. N. Krivorotov, *Nat. Nanotechnol.* **14**, 27 (2019).
- [20] C. Safranski, J. Z. Sun, J.-W. Xu, and A. D. Kent, *Phys. Rev. Lett.* **124**, 197204 (2020).
- [21] J. Železný, Y. Zhang, C. Felser, and B. Yan, *Phys. Rev. Lett.* **119**, 187204 (2017).
- [22] M. Kimata, H. Chen, K. Kondou, S. Sugimoto, P. K. Muduli, M. Ikhlas, Y. Omori, T. Tomita, A. H. MacDonald, S. Nakatsuji *et al.*, *Nature (London)* **565**, 627 (2019).
- [23] M. Naka, S. Hayami, H. Kusunose, Y. Yanagi, Y. Motome, and H. Seo, *Nat. Commun.* **10**, 4305 (2019).
- [24] A. Mook, R. R. Neumann, A. Johansson, J. Henk, and I. Mertig, *Phys. Rev. Res.* **2**, 023065 (2020).
- [25] R. González-Hernández, L. Šmejkal, K. Výborný, Y. Yahagi, J. Sinova, T. Jungwirth, and J. Železný, *Phys. Rev. Lett.* **126**, 127701 (2021).
- [26] S. Wimmer, M. Seemann, K. Chadova, D. Ködderitzsch, and H. Ebert, *Phys. Rev. B* **92**, 041101(R) (2015).
- [27] M. Seemann, D. Ködderitzsch, S. Wimmer, and H. Ebert, *Phys. Rev. B* **92**, 155138 (2015).
- [28] R. Karplus and J. M. Luttinger, *Phys. Rev.* **95**, 1154 (1954).
- [29] J. Smit, *Physica* **21**, 877 (1955).
- [30] L. Berger, *Phys. Rev. B* **2**, 4559 (1970).
- [31] Y. Omori, E. Sagasta, Y. Niimi, M. Gradhand, L. E. Hueso, F. Casanova, and Y. C. Otani, *Phys. Rev. B* **99**, 014403 (2019).

- [32] Y. Koike, S. Iihama, and S. Mizukami, *Jpn. J. Appl. Phys.* **59**, 090907 (2020).
- [33] Y. Hibino, K. Yakushiji, A. Fukushima, H. Kubota, and S. Yuasa, *Phys. Rev. B* **101**, 174441 (2020).
- [34] P. W. Anderson, *J. Appl. Phys.* **37**, 1194 (1966).
- [35] P. Streda, *J. Phys. C: Solid State Phys.* **15**, L717 (1982).
- [36] A. Altland and B. D. Simons, *Condensed Matter Field Theory*, 2nd ed. (Cambridge University Press, Cambridge, 2010).
- [37] G. D. Mahan, *Many-Particle Physics*, 3rd ed. (Springer, Boston, MA, 2000).
- [38] P. M. Levy, *Phys. Rev. B* **38**, 6779 (1988).
- [39] A. Fert and P. M. Levy, *Phys. Rev. Lett.* **106**, 157208 (2011).
- [40] T. Tanaka and H. Kontani, *New J. Phys.* **11**, 013023 (2009).
- [41] Only $\tilde{t}_{k',k}$, and \tilde{G}_k depend on the momentum direction \hat{k} , and the other terms are isotropic with respect to the momentum space. Obviously, $\tilde{t}_{k',k} \propto Y_{2,M}^*(\hat{k}')Y_{2,M}(\hat{k})$ is an even function with respect to \mathbf{k} and \mathbf{k}' as $Y_{L,M}(\hat{k})$ becomes an even function when L is an even number. For \tilde{G}_k , we set the isotropic terms as $\tilde{g}'_k \equiv (\tilde{g}_k^{-1} \pm i\eta_{ss}\tilde{\sigma}_0)^{-1}$, and then expand \tilde{G}_k with respect to $\tilde{t}_{k,k}$ as
- $$\tilde{G}_k = \tilde{g}'_k + n_{\text{imp}}\tilde{g}'_k\tilde{t}_{k,k}\tilde{g}'_k + n_{\text{imp}}^2\tilde{g}'_k\tilde{t}_{k,k}\tilde{g}'_k\tilde{t}_{k,k}\tilde{g}'_k + \dots$$
- The n th general term is proportional to $\{Y_{2,M}^*(\hat{k})Y_{2,M}(\hat{k})\}^n$; therefore, \tilde{G}_k is also an even function with respect to \mathbf{k} .
- Thus, the general terms of the response function vanish as the integration of an odd function, except for the first term ($\delta_{k',k}\delta_{\beta,\alpha}\hat{k}$).
- [42] A. Fert, *J. Phys. F: Met. Phys.* **3**, 2126 (1973).
- [43] A. Fert and A. Friederich, *Phys. Rev. B* **13**, 397 (1976).
- [44] F. Takata, K. Kabara, K. Ito, M. Tsunoda, and T. Suemasu, *J. Appl. Phys.* **121**, 023903 (2017).
- [45] A. Crépieux and P. Bruno, *Phys. Rev. B* **64**, 014416 (2001).
- [46] S. Sadjina, A. Brataas, and A. G. Mal'shukov, *Phys. Rev. B* **85**, 115306 (2012).
- [47] For the code, see <https://bitbucket.org/zeleznyj/linear-response-symmetry/src/master>. To obtain the tensor shape in our model, once we obtain the tensor in a body-centered cubic ferromagnet with $\hat{m} \parallel \hat{z}$ by the code, then we apply additional constraint from the continuous rotational operation.
- [48] We confirmed that the tensor forms of Eq. (25) are compatible with the magnetic Laue groups of $\bar{1}$, $2/m$, $4/m$, $6/m$, $\bar{3}$, $2'/m'$, $m'm'm$, $4/mmm'm'$, $6/mmm'm'$, $\bar{3}1m'$, and $\bar{3}m'1$ in Tables VIII and IX in Ref. [27]. In order to compare them, the indices in Eq. (25) are replaced from (θ, ϕ, m) to (z, x, y) for $2'/m'$, and from (θ, ϕ, m) to (x, y, z) otherwise.
- [49] K. Morawetz, *Phys. Rev. B* **92**, 245425 (2015).